

c2d *Spitzer* IRS spectra of embedded low-mass young stars: gas-phase emission lines

Fred Lahuis^{1,2}, Ewine F. van Dishoeck^{2,3}, Jes K. Jørgensen⁴,
Geoffrey A. Blake⁵, Neal J. Evans II⁶

¹ SRON Netherlands Institute for Space Research, P.O. Box 800, 9700 AV Groningen, The Netherlands

² Leiden Observatory, Leiden University, P.O. Box 9513, 2300 RA Leiden, The Netherlands

³ Max-Planck-Institut für extraterrestrische Physik (MPE), Giessenbachstr. 1, 85748 Garching, Germany

⁴ Centre for Star and Planet Formation, Natural History Museum of Denmark, University of Copenhagen, Øster Voldgade 5-7, DK-1350 Copenhagen K, Denmark

⁵ Division of Geological and Planetary Sciences 150-21, California Institute of Technology, Pasadena, CA 91125

⁶ The University of Texas at Austin, Dept. of Astronomy, 1 University Station C1400, Austin, Texas 78712-0259

Preprint online version: November 2, 2018

ABSTRACT

Context. A survey of mid-infrared gas-phase emission lines of H₂, H₂O and various atoms toward a sample of 43 embedded low-mass young stars in nearby star-forming regions is presented. The sources are selected from the *Spitzer* “Cores to Disks” (c2d) legacy program.

Aims. The environment of embedded protostars is complex both in its physical structure (envelopes, outflows, jets, protostellar disks) and the physical processes (accretion, irradiation by UV and/or X-rays, excitation through slow and fast shocks) which take place. The mid-IR spectral range hosts a suite of diagnostic lines which can distinguish them. A key point is to spatially resolve the emission in the *Spitzer*-IRS spectra to separate extended PDR and shock emission from compact source emission associated with the circumstellar disk and jets.

Methods. An optimal extraction method is used to separate both spatially unresolved (compact, up to a few hundred AU) and spatially resolved (extended, thousand AU or more) emission from the IRS spectra. The results are compared with the c2d disk sample and literature PDR and shock models to address the physical nature of the sources.

Results. Both compact and extended emission features are observed. Warm (T_{ex} few hundred K) H₂, observed through the pure rotational H₂ S(0), S(1) and S(2) lines, and [S I] 25 μ m emission is observed primarily in the extended component. [S I] is observed uniquely toward truly embedded sources and not toward disks. On the other hand hot ($T_{\text{ex}} \geq 700$ K) H₂, observed primarily through the S(4) line, and [Ne II] emission is seen mostly in the spatially unresolved component. [Fe II] and [Si II] lines are observed in both spatial components. Hot H₂O emission is found in the spatially unresolved component of some sources.

Conclusions. The observed emission on ≥ 1000 AU scales is characteristic of PDR emission and likely originates in the outflow cavities in the remnant envelope created by the stellar wind and jets from the embedded young stars. Weak shocks along the outflow wall can also contribute. The compact emission is likely of mixed origin, comprised of optically thick circumstellar disk and/or jet/outflow emission from the protostellar object.

Key words. Stars: formation - Stars: low-mass - Stars: protostars - ISM: jets and outflows - ISM: lines and bands - ISM: photon-dominated region (PDR)

1. Introduction

Understanding the nature of deeply embedded protostars is a major challenge in the study of low-mass star formation. In its earliest stages, a young star is embedded in its natal envelope of cold gas and dust, prohibiting direct detection with optical and near-IR instruments. During the evolution of such protostars the envelope is dissipated partly due to the ongoing accretion onto the central star and disk and partly due to the action of the outflows driven by such stars. This embedded phase lasts only a short time, $\sim 6 \times 10^5$ yr (Evans et al. 2009), but is critical for the subsequent evolution of the star: it is the phase in which the final mass of the star, the overall mass of the circumstellar disk (and thus its ability to form planets), and the initial physical and chemical structure of the disk are determined.

The envelope surrounding young stars is subjected to highly energetic phenomena, in particular X-rays and UV radiation and streams of gas ejected from the star-disk boundary region. Both the slow and high velocity gas can shape the protostellar envelopes on a variety of spatial scales. The related physical processes, outlined below, have a strong impact on the physical structure and the molecular and atomic contents of the surrounding material. Mid-infrared spectroscopy, the central focus of this paper, provides a powerful tool to characterize and quantify the nature and energetics of these interactions as well as the composition and temperature structure of the material involved.

Based on previous infrared and submillimeter data, a general picture has emerged of the structure of embedded young stellar objects (YSOs) (e.g., Young et al. 2004; Jørgensen et al. 2002, 2005; Chiang et al. 2008; Tobin et al. 2010). Take as an example the isolated source HH 46 IRS (IRAS 08242-5050) imaged with the *Spitzer* Space Telescope (see Noriega-Crespo et al. 2004;

Send offprint requests to: Fred Lahuis
e-mail: F.Lahuis@srn.nl

Velusamy et al. 2007, and references cited) and studied in detail with submillimeter molecular lines as well as dust continuum emission (see summary in van Kempen et al. 2009b). The young star is surrounded by a roughly spherically symmetric envelope with a mass of $\sim 5 M_{\odot}$ and a power-law density structure, with $n(\text{H}_2) \approx 10^6 \text{ cm}^{-3}$ at 1000 AU from the star, decreasing to $\sim 10^5 \text{ cm}^{-3}$ at ~ 7000 AU. The infrared images reveal prominent red- and blue-shifted outflow lobes traversing the envelope with an opening angle up to 110° and continuing out to 0.2 pc. These outflow lobes are produced by jets and/or wide angle winds propagating at speeds up to 200 km s^{-1} , which interact with the surroundings and create a shocked shell of material that is entrained and propelled outward at some speed (e.g., Bally et al. 2007; Ray et al. 2007; Shang et al. 2007). The most prominent example of this interaction is the bow shock at the tip of the outflow. In addition, blobs of shocked warm gas and dust are seen at various locations along the outflow axis, which may be internal shocks in the (variable) wind or jet itself. Similar physical structures are expected for other embedded YSOs, although the densities at 1000 AU are up to an order of magnitude lower for sources with lower mass envelopes (Jørgensen et al. 2002).

The outflow cavities create a low-extinction pathway for ultraviolet (UV) photons produced in the accreting gas column at the star-disk boundary layer to escape out to much further distances (Spaans et al. 1995; Bruderer et al. 2009b,a) than possible in a purely spherical symmetry (e.g. Stäuber et al. 2004). For a UV luminosity of $0.1 L_{\odot}$ typical of low-mass YSOs, the enhancement of the UV radiation field with respect to the general radiation field is about $G_0 \approx 10^4$ at 100 AU. Moreover, UV radiation is created along the outflow by the shocks themselves, especially by the higher velocity *J*-type shocks (Hollenbach & McKee 1989; Neufeld & Dalgarno 1989). Evidence for UV enhancements G_0 of a few hundred out to 0.1 pc have recently been inferred from observations of narrow high-*J* CO submillimeter emission lines surrounding the outflow cavity walls (van Kempen et al. 2009b,a, see their Fig. 13). Thus, the *Spitzer* IRS slit of about $5 - 10''$ will pick up emission from gas with a range of densities from $10^4 - 10^7 \text{ cm}^{-3}$, exposed to UV radiation with $G_0 \approx 10^2 - 10^4$, and subjected to shocks with velocities up to several hundred km s^{-1} for typical cloud distances of 100 – 400 pc.

The consequences of UV radiation impacting on dense gas have been studied for decades through models of so-called Photon-Dominated Regions (or PhotoDissociation Regions, PDR) (Tielens & Hollenbach 1985b,a; Hollenbach et al. 1991; Hollenbach & Tielens 1999). In the PDR layers closest to the UV source most molecular material is dissociated and the atomic species with ionization potential below 13.6 eV are ionized. This layer is characterized by bright fine structure lines such as [O I], [Fe I], [Fe II] and [Si II]. [S I] is never strong as most of the sulfur is in the form of S^+ in the warm PDR. At deeper layers, H_2 can survive, yet remains highly excited, resulting in strong pure rotational H_2 lines (e.g. Kaufman et al. 2006, applied to regions of massive star-formation).

Shocks impacting the surrounding envelope can be divided into two types: *J*- and *C*-type shocks. The so-called dissociative *J*-shocks (Draine & McKee 1993; Hollenbach 1997; Walmsley et al. 2005) heat the gas up to 10^5 K. Infrared emission comes from the dense hot post-shock gas in which most of the molecular material is still dissociated and a large fraction of the atoms are ionized resulting in strong emission lines of singly and doubly ionized atoms (e.g., [Fe II] 26 and $35 \mu\text{m}$, [Ni II] $6.6 \mu\text{m}$). This includes atoms which cannot

be directly photoionized by photons with energies < 13.6 eV such as the [Ne II] $12.8 \mu\text{m}$ line (Hollenbach & McKee 1989; Hollenbach & Gorti 2009). Further downstream, molecular hydrogen forms in the cooling gas and strong high-*J* pure rotational line emission is expected. [Ne II] emission is strong only in high velocity shocks ($v_s > 70 \text{ km s}^{-1}$), while the strength of other fine structure lines (e.g. [S I] $25 \mu\text{m}$, [Fe I] $24 \mu\text{m}$ and [Cl I] $11.4 \mu\text{m}$) does not strongly depend on the shock velocity (see Hollenbach & McKee 1989, for details). Note that these fast shocks imply travel times through the envelope of only ($< 10^4$ yrs), unless the material is significantly slowed down by the interaction. For the so-called non-dissociative *C*-shocks (e.g. Neufeld & Kaufman 1993; Kaufman 1995; Kaufman & Neufeld 1996), the temperatures never become high enough to dissociate molecules; these shocks show strong lines from excited H_2 , CO, H_2O and OH (e.g. Kaufman & Neufeld 1996).

To date, PDR and shock models have mostly been applied to the general interstellar medium (ISM) near massive young stars or supernova remnants. Previous observations of low mass young stellar objects (YSOs) using ground-based observatories or the ISO-SWS instrument (de Graauw et al. 1996; van den Ancker 1999) either lacked the sensitivity to observe the emission lines or the spatial resolution to separate the various emitting regions (see van Dishoeck 2004, for an overview). The sensitive InfraRed Spectrograph (IRS) (Houck et al. 2004) on board the *Spitzer* Space Telescope (Werner et al. 2004) brings the detection of the mid-IR H_2 pure rotational and atomic fine structure lines within reach for young Sun-like stars in nearby star-forming regions. The combination of high sensitivity, moderate spectral resolution $R = \lambda/\Delta\lambda = 600$, and modest spatial resolution makes *Spitzer* well suited for the study of the gas in the ISM around low-mass young stars in the nearest ($\lesssim 300$ pc) clouds. Moreover, the *Spitzer* aperture allows us, using an optimal extraction method, to disentangle both spatial components from the IRS echelle and long-slit spectral images down to scales of a few arcsec, better than can be achieved with single-dish millimeter telescopes. The combination of line fluxes, line ratios and spatial extent can help to identify the dominant heating processes – PDR or shock-driven – taking place, and thus the physical structure of the envelope on scales of a few hundred to a few thousand AU. The *Spitzer* data thus complement traditional studies with (sub)millimeter telescopes.

Theory predicts that disks are established early in the embedded phase of star formation, as the inevitable byproduct of the collapse of a rotating core (e.g. Terebey et al. 1984; Cassen & Moosman 1981). Such ‘young’ disks, some of which show Keplerian velocity patterns, have been detected in submillimeter interferometry data (e.g. Keene & Masson 1990; Lommen et al. 2008; Jørgensen et al. 2009), but little is known about their physical and chemical structure. Detailed models of X-ray and UV irradiation of disk surface layers exist for more evolved pre-main sequence stars where the envelopes have been completely dissipated (Bergin et al. 2007; Gorti & Hollenbach 2008; Woitke et al. 2009; Bergin 2009). *Spitzer* observations have revealed surprisingly rich spectra of such protoplanetary disks, with the lines seen either in absorption in a near edge-on geometry (Lahuis et al. 2006) or in emission (Carr & Najita 2008; Salyk et al. 2008). Lines from H_2O , HCN, C_2H_2 , CO_2 and OH have been detected, indicating hot molecular gas at temperatures of $\sim 500 - 1000$ K arising from the inner few AU of the disk. This hot gas is also seen in ground based CO infrared data (e.g. Najita et al. 2003; Blake & Boogert 2004). Such disks show various atomic transitions as well, most prominently the [Ne II] $12.8 \mu\text{m}$ line (Lahuis et al. 2007b; Pascucci et al. 2006;

Espaillat et al. 2007) (see also models by Meijerink et al. 2008). An interesting question is therefore whether young disks in the embedded phase studied here have similar spectra as the more evolved disks, or whether they show additional features, for example due to the accretion shock of material falling on to the disk (Pontoppidan et al. 2002; Watson et al. 2007).

We present here an overview of the mid-IR gas-phase lines detected in embedded sources, including class 0 and class I sources observed in the *Spitzer* legacy program “From Molecular Cores to Planet Forming Disks” (“Cores to Disks” or c2d) (Evans et al. 2003). This program has collected a large sample of IRS spectra toward sources in the nearby Chamaeleon, Lupus, Perseus, Ophiuchus, and Serpens star-forming regions. High- S/N spectra have been obtained within the $5 - 38 \mu\text{m}$ range for 226 sources at all phases of star and planet formation up to ages of ~ 5 Myr, of which 61 are presented here. Many of the sources are also included in the series of papers discussing the ice features in the c2d sample (Boogert et al. 2008; Pontoppidan et al. 2008; Öberg et al. 2008). In Sections 2 and 3 the source selection and data reduction are explained. In Section 4 the observed atomic fine-structure and H_2 emission lines and the derived parameters are presented. Section 5 reviews the results within the context of PDR and shock heating and by comparing the embedded sources in the present sample with the more evolved disk sources in the larger c2d program that have been discussed in (Lahuis et al. 2007b).

2. Observations

The data presented in this study were selected from the sample of IRS spectra observed within the *Spitzer* c2d legacy program. The c2d IRS component consists of two programs of comparable size, referred to as the first- and second-look programs. The first-look program (PID #172) was restricted primarily to known low-mass young stars, embedded YSOs and pre-main-sequence stars with disks with stellar masses $M < 2 M_\odot$ and ages $\lesssim 5$ Myr, and a sample of background stars. A few Herbig Ae stars were included as well. The c2d source selection criteria were defined to be complementary to those of the *Spitzer* legacy program “The Formation and Evolution of Planetary Systems” (FEPS, Meyer & the entire FEPS team 2007). The second-look program (PID #179) was, for the most part, devoted to IRS follow-up spectroscopy of sources discovered in the IRAC and MIPS mapping surveys, including a newly discovered cluster of young stars in Serpens (Harvey et al. 2006). For all first-look observations, the integration times for the short-high (SH) and long-high (LH) modules ($R = 600$, $10 - 37 \mu\text{m}$) were chosen such that theoretical signal to noise ratios (S/N s) of at least 100 and 50 on the continuum were obtained for sources brighter and fainter than 500 mJy, respectively. Deeper integrations were not feasible within the c2d program. Spectra taken using the short-low (SL) or long-low (LL) modules ($R = 60 - 120$, $5 - 14 \mu\text{m}$ and $14 - 38 \mu\text{m}$ respectively) always reach theoretical S/N ratios greater than 100. For the second-look IRS targets similar S/N limits were obtained wherever possible. However, since the second-look contained a number of very weak sources (down to a few mJy) this was not always achieved.

The 61 sources presented in this paper were all selected from those showing the $10 \mu\text{m}$ silicate band in absorption. This criterion includes embedded Stage I sources (as defined by Robitaille et al. 2006) plus obscured disks (e.g. edge-on stage II sources ($i \gtrsim 65$ degrees), Crapsi et al. 2008), such as CRBR 2422.8-3423 (Pontoppidan et al. 2005) and IRS 46 (Lahuis et al. 2006). All of the sources have a rising SED in the

mid-IR, the characteristic for Class I YSOs. The selected sources are listed in Table 1 which gives the basic observation and source parameters plus the adopted distances. Note that in most cases, it is not possible to determine whether the infrared source is dominated by an envelope or a disk without additional spatially resolved far-infrared and/or (sub)millimeter data. A subsequent submillimeter line study by van Kempen et al. (2009c) of Ophiuchus L1688 has been able to separate truly embedded YSOs (Stage I) from obscured disks or confused sources. Of the 61 sources, 43 are found to be truly embedded; 10 sources are obscured stage II sources (edge-on disks or disks behind large columns of gas and dust); and for 8 sources the classification is unclear. Some obscured disks were not included in the c2d IRS survey of gas-phase lines in disks (Lahuis et al. 2007b), so their data are presented here for completeness, but are analyzed separately.

3. Data reduction

The c2d reduction pipeline (Chapter 3 of Lahuis 2007, and the c2d-IRS delivery documentation¹) was used to reduce the IRS data, starting from the S15, S16 and S17 archive data. The same c2d pipeline products as included in the final c2d Legacy data delivery² were used for the spectral line analysis (see Sec. 3.4). Most of the analysis focused on the SH and LH data, since for intrinsically narrow lines the SL and LL data are generally limited by the low line/continuum ratio. The SL data were included in the analysis to search for higher-excitation $\text{H}_2 v = 0$ lines, in particular the S(3) transition.

If a module was not included in the c2d observation the *Spitzer* archive was searched for additional pointed observations to supplement the missing data. For some sources data are missing, in particular SL. For example, Serp-SMM3 and Serp-SSM4 have not been observed in the low resolution staring mode (see Table 1) and therefore do not cover the higher rotational ($J \geq 3$) H_2 lines. Some of these are covered through mapping observations, however these are not included in this analysis.

The c2d disk sources (Lahuis et al. 2007b) are used for comparison with the embedded sources and have all been reprocessed using the same reduction to provide the data presented in this paper. Compared with Lahuis et al. (2007b) this has led to an increased number of detection for the disk sources, most importantly new detections of [Ne II] (Güdel et al. 2010) and [Fe II].

3.1. Separating disk and cloud emission – optimal extraction

A major concern when studying YSOs in the mid-IR is the possible contribution of extended (envelope or local cloud), yet structured, emission in the sometimes complex star-forming regions. Variations in the spatial distribution of the emission (see Figure 1), both in the continuum and in spectral lines, limit the use of ‘sky’ observations to correct for extended emission components. For this reason the c2d team developed an optimal extraction algorithm for IRS pointed observations starting from the SSC Archive droop products.

The *Spitzer* slit size is $\sim 4 - 5''$ for the SH module ($10 - 19.5 \mu\text{m}$) and $\sim 7 - 10''$ for the LH module ($19 - 37 \mu\text{m}$). At a distance of 100 pc this corresponds to physical sizes of $\sim 400 - 500$ AU and $\sim 700 - 1000$ AU, respectively. The clouds

¹ http://data.spitzer.caltech.edu/popular/c2d/20061201_enhanced_v1/Documents/C2D_Spectr_Expl_Supp.pdf

² The c2d legacy data are accessible at <http://ssc.spitzer.caltech.edu/legacy/c2dhistory.html>.

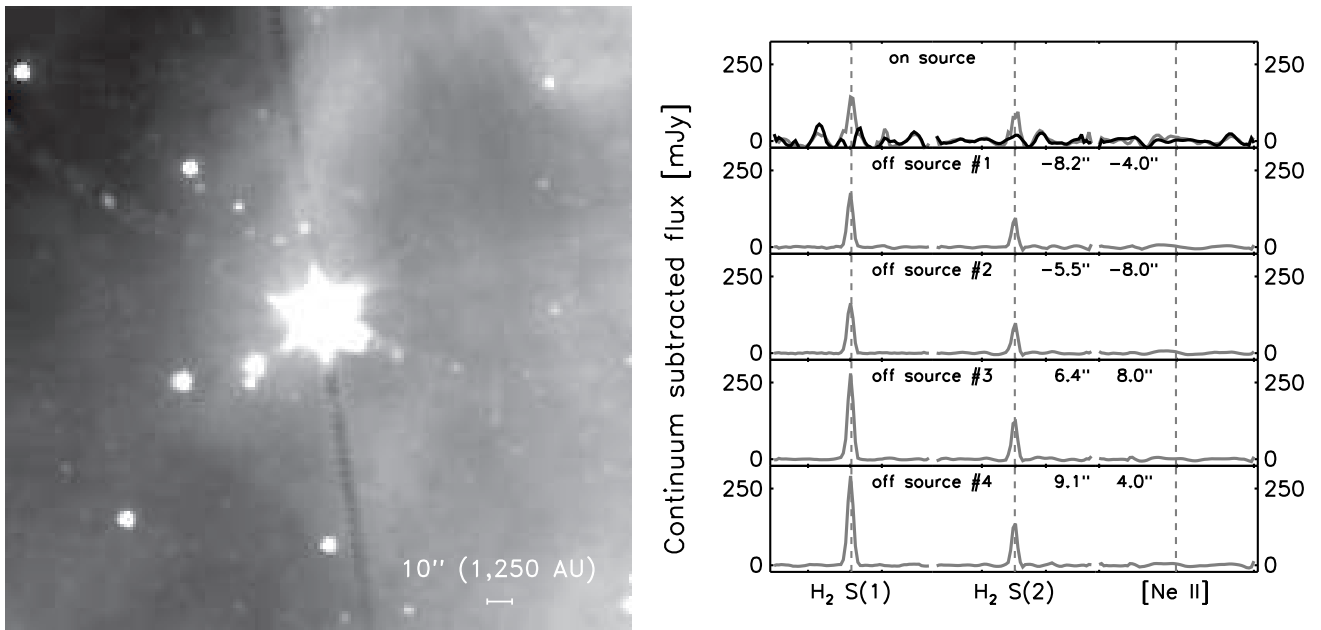


Fig. 1. *Spitzer*-IRS SH minimap observed around VSSG1 in Ophiuchus. The left plot displays a *Spitzer*-IRAC image at $4.5\ \mu\text{m}$ (including the high excitation H_2 S(9), S(10) and S(11) lines) showing the star plus diffuse extended emission. The right plot shows the spectrum observed in the on-source *Spitzer*-IRS observation (top panel) and the off-source spectra obtained with the *Spitzer*-IRS minimap. In gray the total observed emission and in black the unresolved source emission toward VSSG1 are presented. Virtually all H_2 S(1) $17.03\ \mu\text{m}$ and S(2) $12.28\ \mu\text{m}$ emission is extended in this source. $[\text{Ne II}]$ $12.81\ \mu\text{m}$ emission is absent toward VSSG1.

observed in the c2d program are assumed to be located at distances ranging from 125 pc (Ophiuchus) to 260 pc (Serpens) increasing the physical area observed. The full IRS aperture in the SH and LH spatial direction is $\sim 2.5 - 3$ times larger than the beam size. At the observed cloud distances this means that the aperture probes physical scales of several thousand AU. This makes it ideally suited for detecting warm or shocked H_2 emission from the extended (remnant) envelope, outflows, or the diffuse local cloud emission. For the sources studied in this work however the local cloud emission will potentially confuse compact disk emission. Distinguishing between compact (disk and inner envelope) and extended (remnant envelope, outflow, or diffuse cloud) emission is therefore of vital importance for studying the emission lines originating in the circumstellar disks or the cores of jets/winds launched on small scales.

The optimal extraction developed by the c2d team uses an analytical cross-dispersion point spread function (PSF) to describe the source profile (see Figure 2). The PSF plus an extended emission component are fit to the observed crosstalk or straylight corrected echelle (SH and LH) and longslit (SL and LL) images. The PSF is described by a sinc function with a harmonic distortion component (resulting in a significant broadening of the profile wings as shown in Figure 2). The wavelength dependence of the PSF parameters (the order trace, the width, and the harmonic distortion) are characterized using a suite of high- S/N calibrator stars. The extended emission component is approximated by a low order polynomial folded with the flatfield cross-dispersion profile. The flux calibration is derived from the calibrator stars using Cohen templates and MARCS models (Decin et al. 2004) provided through the *Spitzer* Science Center. More details about the characterization and calibration of the c2d optimal extraction is presented in Chapter 3 of Lahuis (2007) and in Lahuis et al. (2007b). The optimal extraction returns the total flux (the source flux plus extended emission in the IRS beam) along with an estimate of the extended emission component with

error estimates. The S/N of the extended emission component can vary significantly depending on the quality of the raw image data and on deviations of the extended emission from the assumed uniformity across the IRS slit.

Source sizes as listed in Table 2 are determined from the width of the observed cross dispersion source profile (see Figure 2) deconvolved with the average width of the standard star source profiles.

3.2. SH mini maps

In an early phase of the c2d project H_2 and $[\text{Ne II}]$ lines were detected toward some of the c2d sources. Initial results using an early version of the c2d optimal extraction, from IRS starting observations, suggested some of the observed emission to be extended. Therefore, as part of the second-look program, follow-up mini-maps were taken using the SH module to check for extended emission at offsets positions of $\sim 10\text{--}15''$ with respect to the sources. Five maps were defined to include off-source observations around eight sources. Figure 1 shows the results toward VSSG1, whereas Lahuis et al. (2007b) (their Figure 1) show the results toward the disk sources Sz 102 (Krautter’s star), Haro 1-17, and EC 74. Here, Figure 1 presents the observed H_2 0-0 S(1), S(2), and $[\text{Ne II}]$ emission from the first-look on-source observations together with the off-source observations from the second-look mini maps. It is seen that most of the H_2 emission is extended and that it may vary on scales of a few $''$, especially for the S(1) line. However, some emission lines such as $[\text{Ne II}]$ are typically seen to be limited to the source itself (Lahuis et al. 2007b).

The mini map results confirmed the results from the c2d optimal extraction procedure. It showed that it was possible to reliably extract the extended emission component from the IRS staring observations. The procedure was further developed and

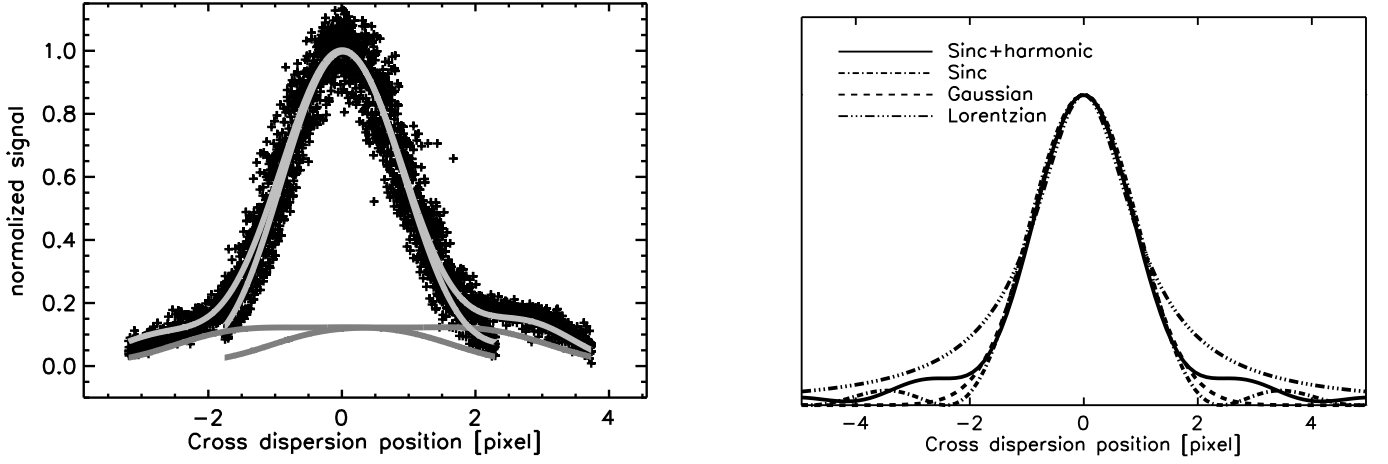


Fig. 2. Illustration of the *Spitzer* IRS cross dispersion profile used in the optimal extraction (see Sec. 3.1). The left plot shows a fit to the data of an IRS SH order of a pointsource with a moderate but clear sky component in the IRS spectra. The SH pixel size is ~ 2.3 arcsec. For LH the profile is similar but the pixel size is ~ 2 times larger. The observed data are plotted with black plusses. Overplotted are the total profile fit (source plus extended emission) and the included extended component. The shape of the extended emission reflects the IRS flatfield of the (for this source) assumed uniform extended emission. The right plot shows a comparison of an IRS PSF profile (Sinc plus harmonics) for a pointsource compared to the profiles of an undistorted Sinc, a Gaussian, and a Lorentzian profile with the same FWHM. Note the significant variation in the strength and shape of the profile wings. The correct characterization of both the width and the wings of the profile for all IRS orders is essential for extracting the proper source and sky spectra.

has since been used in several studies, e.g. Lahuis et al. (2007b); Geers et al. (2006); Boersma et al. (2008).

3.3. 1-D spectra

After extraction, the 1-D spectra are corrected for instrumental fringe residuals (Lahuis & Boogert 2003), order matching (by a few %) is applied, and a pointing flux-loss correction is performed on the compact source component (see Chapter 3 of Lahuis 2007). Pointing offsets up to a few arcsec can have a noticeable impact on the derived fluxes of lines observed with the SH and SL modules, e.g. H_2 0-0 S(1), S(2), [Ne II], and [Ne III]. For example, dispersion offsets within the nominal 3σ pointing uncertainty of *Spitzer* ($\sim 1''$ for medium accuracy pickup) can lead to SL and SH wavelength dependent flux losses up to $\sim 10\%$. Fortunately for all targets a combination of modules is available which permits us to apply a reliable pointing flux loss correction.

3.4. Spectral analysis

The IRS SH and LH modules cover the positions of the three lowest pure rotational lines of H_2 , fine structure emission from [Ne II] ($12.8 \mu\text{m}$), [Ne III] ($15.55 \mu\text{m}$), [Fe I] ($24 \mu\text{m}$), [Fe II] (17.9 and $26.0 \mu\text{m}$), [S I] ($25.25 \mu\text{m}$), [S III] ($18.7 \mu\text{m}$), [Si II] ($34.8 \mu\text{m}$), and hundreds of H_2O transitions at a resolving power of $R = \lambda/\Delta\lambda = 600$. The IRS SL module covers the higher rotation H_2 lines up to $J_l = 7$ at a resolving power of $60 - 120$. Line fitting and flux integration is done to all H_2 and atomic lines using routines from OSIA³.

The extended spectral component (either the estimate or a Gaussian fit depending on the final S/N in the corrected spectrum) is subtracted from the total spectrum to isolate the spatially

unresolved component. Spectral lines are fit to obtain line fluxes for both spatial components. Uncertainty estimates, as listed in Tables 3 and 4, are derived from the residuals after line fitting, or, in the absence of a spectral line, using the line width derived from the instrumental resolution. An uncertainty estimate is derived for both the extended and compact line fit and combined. As a result, the $1-\sigma$ uncertainty estimates can vary widely for sources with a similar continuum flux and integration time. This may, for example, be the result of the presence of artifacts resulting from hot pixels or small variations in the extended emission which are not fully accounted for in the spectral extraction.

Typical mean 4σ uncertainties prior to subtraction of the extended component for the high resolution modules range from $\sim 0.1-2 \times 10^{-15} \text{ erg cm}^{-2} \text{ s}^{-1}$ with extremes of $\sim 5 \times 10^{-17} \text{ erg cm}^{-2} \text{ s}^{-1}$ and $\sim 1 \times 10^{-14} \text{ erg cm}^{-2} \text{ s}^{-1}$. Note that the uncertainties used in this paper include an extended component uncertainty.

4. Results

A search for the major atomic fine-structure lines and H_2 lines in the *Spitzer*-IRS wavelength range has been performed for all 61 sources in our sample. Line detections are shown in Figures 3 and 4 for the embedded sources and described in Sections 4.1 and 4.2. In Figure 5 the measured line strengths and upper limits, converted to solar luminosities, are shown as function of L_{IR} (the continuum luminosity between $\lambda = 12.8 - 15.5 \mu\text{m}$), see Section 4.4. Figure 6 shows the ratios and ratio limits for a number of lines. Lines of molecules H_2O , C_2H_2 , HCN and CO_2 have also been searched for and are discussed in Section 4.3.

For both the atomic lines and those of H_2 the observed upper limits are in most cases of the same magnitude as the median line fluxes of the detections (see Figure 5). It is therefore likely that for most sources emission in one or more lines will be present but has gone undetected. The upward trend observed in the upper limits above an IR luminosity of $\sim 10^{-3} L_\odot$ is the result of the

³ OSIA is a joint development of the ISO-SWS consortium. Contributing institutes are SRON, MPE, KUL and the ESA Astrophysics Division. <http://sws.ster.kuleuven.ac.be/osia/>

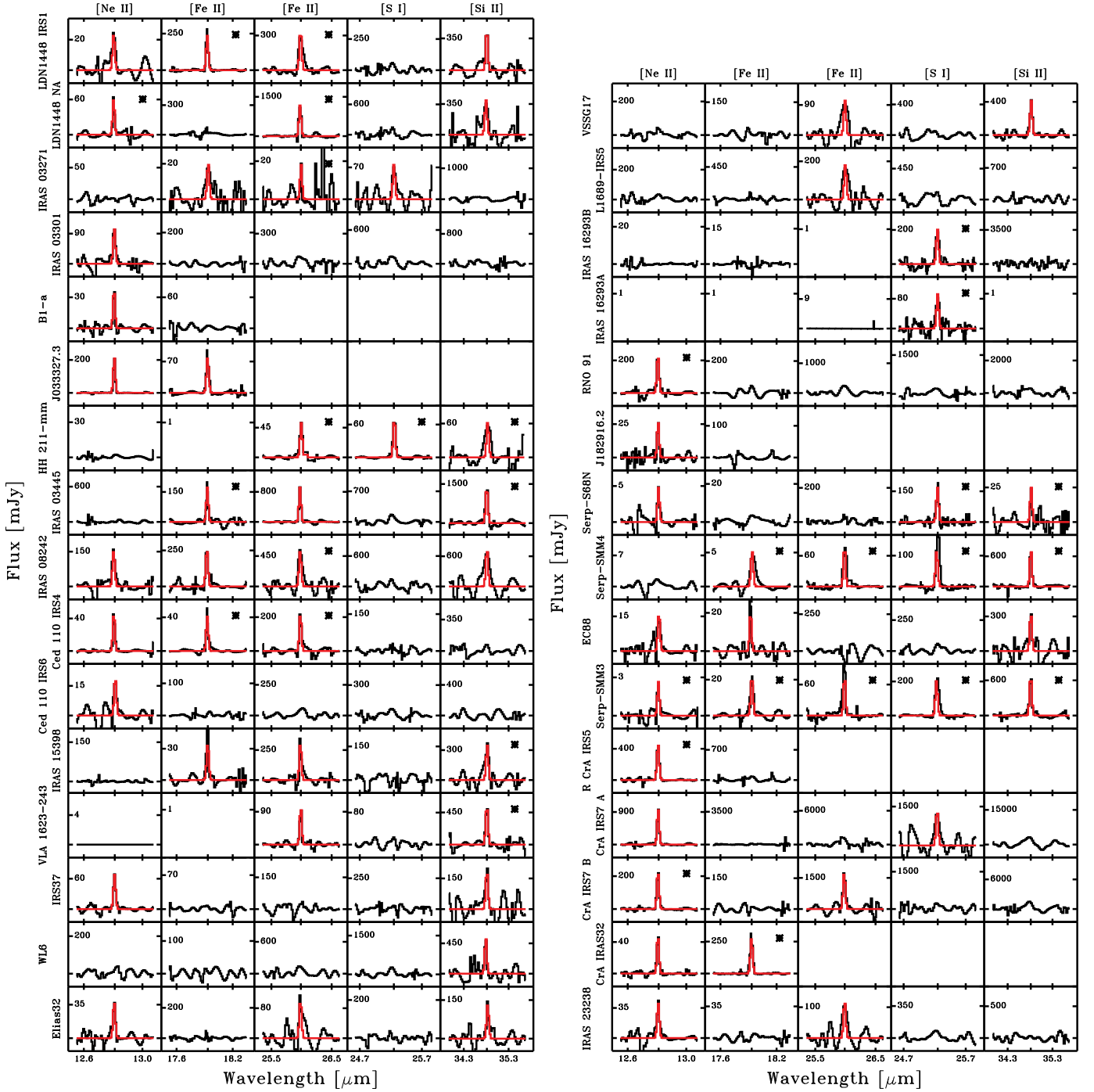


Fig. 3. Detections of [Ne II], [Fe II], [S I] and [Si II] at the $\geq 4\sigma$ level toward the c2d sample of embedded YSOs. Overplotted in red is a Gaussian fit to the observed spectrum. Sources indicated with a star show evidence of a (partial) contribution of extended emission to the total line flux.

dominance of target shot noise in the IRS detector noise at higher source signals.

4.1. Atomic fine-structure lines

Figure 3 shows all 4σ detections of atomic lines. One or more of the [Ne II], [Fe II] 18 and $26\mu\text{m}$, [S I], and [Si II] emission lines are observed toward $\sim 2/3$ of the 43 embedded sources. The measured line fluxes of the extended and compact components and the upper limits are listed in Table 3. Of the sources with line de-

tections $\sim 30\%$ show emission from more than one line. Emission of most atomic lines is observed as both compact and extended emission.

4.2. Molecular hydrogen

Figure 4 shows all 4σ H_2 emission line detections toward the 43 embedded sources in our sample. Emission from one or more H_2 lines observable with the *Spitzer*-IRS (S(0) to S(7)), has been detected toward 36 out of 43 sources, with 31 out of 43 showing

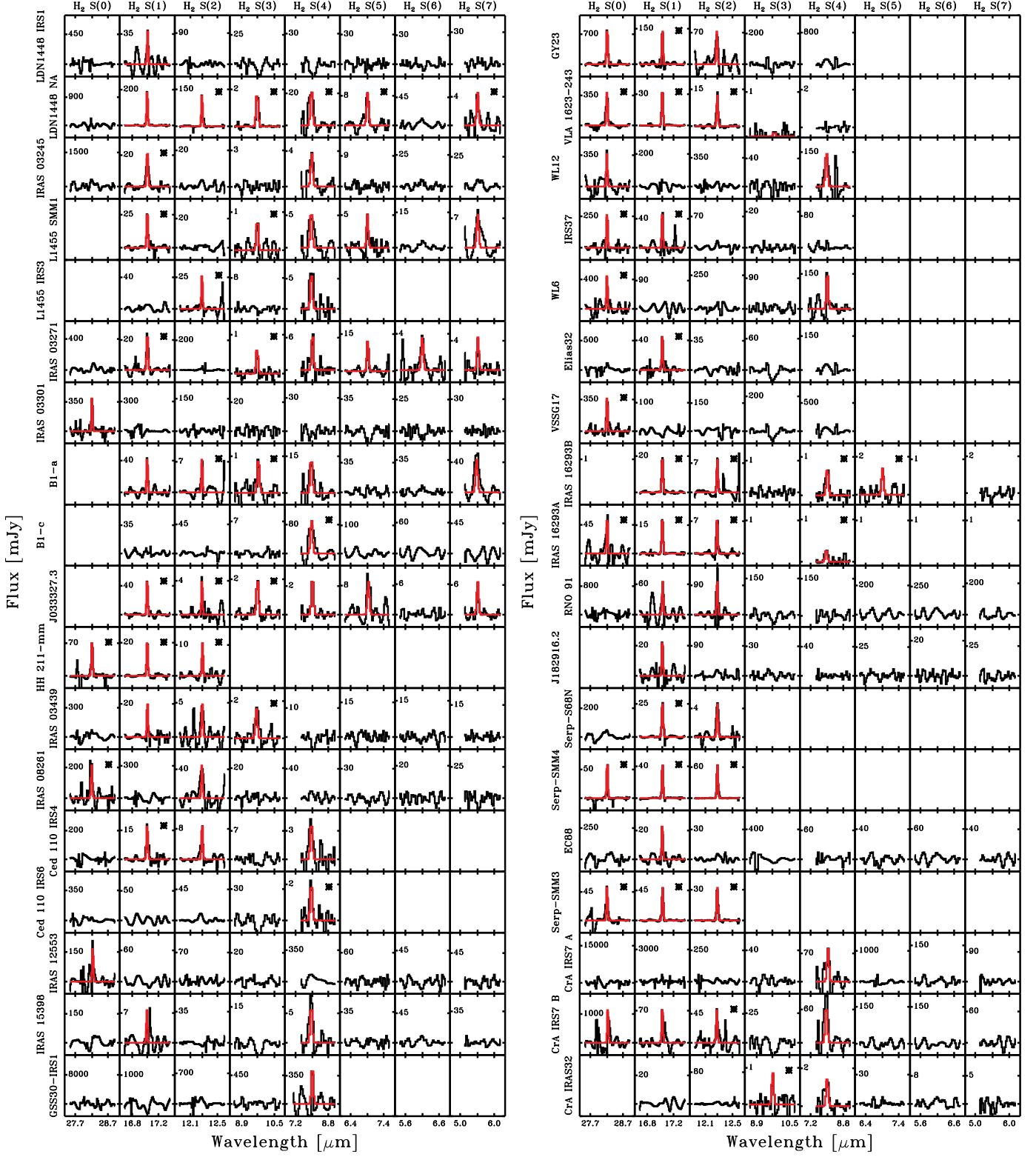


Fig. 4. Detections of H₂ emission lines at the $\geq 4\sigma$ level toward the c2d sample of embedded YSOs. Overplotted in red is a Gaussian fit to the observed spectrum. Sources indicated with a star show evidence of a (partial) contribution of extended emission to the total line flux.

low- J lines and 19 out of 43 high- J lines. The H_2 line fluxes for the compact and extended components and the line flux upper limits are listed in Table 4. The warm gas traced by the low- J lines is observed primarily in the extended component while the hot gas probed by the high- J lines is observed mostly in the compact component.

The warm gas ($T_{\text{ex}} \lesssim 700$ K) traced by the lower rotational lines ($J_l \leq 2$) is mostly extended, except for a few cases. Hot ($T_{\text{ex}} \sim 1000 - 1500$ K) gas is traced by the higher rotational lines ($J_l \geq 4$). For $J_l \geq 5$ no estimate of extended emission is available because the IRS is spatially undersampled at these wavelengths and the usability of the optimal extraction is limited. Mapping observations (e.g. Neufeld et al. 2009) show that, in general, the H_2 high- J lines have a similar distribution to the lower excitation lines. Since most of the $J_l = 4$ detections show no strong signs of an extended emission component, we assume all hot H_2 emission to have a compact origin.

In the simplest analysis, the H_2 excitation is assumed to be in local thermal equilibrium (LTE) (e.g., Thi et al. 2001) with an ortho-to-para ratio determined by the kinetic temperature of the gas (following Sternberg & Neufeld 1999). For gas temperatures 100, 150, and ≥ 200 K, the ortho-to-para ratios are 1.6, 2.5, and 3, respectively. Assuming optically thin emission, the integrated flux of a rotational line $J_u \rightarrow J_l$ for a given temperature T_{ex} is

$$F_{ul}(T_{\text{ex}}) = \frac{hc}{4\pi\lambda} N(H_2) A_{ul} x_u(T_{\text{ex}}) \Omega \text{ erg s}^{-1} \text{ cm}^{-2}, \quad (1)$$

where λ is the wavelength of the transition, $N(H_2)$ the total column density, A_{ul} the spontaneous transition probability, and Ω the source size. For high enough densities ($n > 10^3 \text{ cm}^{-3}$), the population x_u follows the Boltzmann law

$$x_u(T_{\text{ex}}) = \frac{g_N(2J_u + 1)e^{-E_J/kT_{\text{ex}}}}{Q(T_{\text{ex}})} \quad (2)$$

where E_J is the energy of the upper level, g_N is the nuclear statistical weight (1 for para and 3 for ortho H_2), and $Q(T_{\text{ex}})$ the partition function for the given excitation temperature T_{ex} .

Using the above equations, excitation temperatures, column densities and H_2 gas masses, or limits on these, can be derived from the observed line fluxes and upper limits. A source size has to be known or assumed to derive column densities. Observations of multiple H_2 lines in PDRs and shocks typically show multiple temperature components (van den Ancker et al. 1999; Habart et al. 2005), e.g. a warm (T_{ex} of a few 100 K) and a hot ($T_{\text{ex}} \sim 1000$ K or higher) component. In our data, often only a few lines per source are detected. If $J_l < 2$ lines are detected, a (limit of the) temperature of the warm gas is derived. For a few sources more than one of these lines are detected in the extended component. The derived temperatures vary from 85 to 120 K with uncertainties of ~ 20 K. Therefore we adopt a temperature of 100 K for the warm component for all sources. If two or more higher excitation lines ($J_l > 2$ and higher) are detected a temperature for the hot component is derived; otherwise a temperature of 1000 K is adopted. This is done for both spatial components. For some sources multiple H_2 lines are detected allowing a temperature estimate to be made. Temperatures for the hot component, varying from $\sim 500 - 1500$ K, are observed (see Figure 7) in both spatially extended and compact emission. In the analysis no extinction correction is applied and only H_2 is included in the mass calculation.

The column density averaged over the IRS aperture is derived using above equations. For all compact source emission

the source size is smaller than the IRS aperture (Sec. 3). Since this is unknown, a typical size $r = 50$ AU is adopted (gas masses up to a few 10^{-3} Jupiter masses, see below and Figure 8, give an upper limit to the emitting area of 50 AU assuming a density $n \gtrsim 10^5 \text{ cm}^{-3}$). The fitted or adopted excitation temperature plus the J_{up} column densities provide the total column density for that temperature, which in turn gives the total H_2 gas mass, $M_{H_2} = \pi r^2 \times N \times 2m_H/M_J$ with $m_H = 1.674 \cdot 10^{-24}$ gr and $M_J = 1.9 \cdot 10^{30}$ gr, excluding a mass contribution by He. Note that the derived column density scales as $1/r^2$ while the derived gas mass is independent of the adopted beam and/or source size. Therefore the derived column densities can only be used as order of magnitude estimates and are listed for both the warm and hot gas in Table 5. Figure 8 shows the H_2 mass distribution of the warm ($T_{\text{ex}} = 100$ K) and hot ($T_{\text{ex}} = 1000$ K) components for the truly embedded sources. H_2 masses of a few Jovian masses for the warm gas and a few milli-Jovian masses for the hot gas are observed. Hatched bars include all sources where H_2 is detected.

4.3. Molecular emission

Features of H_2O , C_2H_2 , HCN and CO_2 emission are searched for in the full sample. Detecting these species is difficult because the emission features are generally weak and ride on top of a strong mid-IR continuum. H_2O emission is most easily detected as the spectra contain a large number of both spectrally unresolved and blended emission lines across the complete IRS-SH spectral range. Thus, a full spectral range correlation can be applied. Detecting C_2H_2 , HCN and CO_2 is more difficult because only the Q-branches can be observed (P- and R-branch lines are undetectable at the IRS resolution). The Q-branches are, moreover, weak and partially blended with H_2O lines, as seen for example in the spectra of VSSG17 and L1689 IRS5 spectra in Figure 9 where the C_2H_2 , HCN and CO_2 Q-branch positions are marked.

Toward 12/43 truly embedded sources spatially unresolved H_2O emission is positively identified and the presence of C_2H_2 , HCN and CO_2 is, by visual inspection, observed toward a small number of sources (see, e.g., the spectrum of VSSG17 in Figure 9). Toward 4 sources H_2O is clearly detected in both the optimal extraction and the full aperture extraction spectra. For 11 more sources H_2O is positively detected in the optimal extraction spectrum and tentatively detected in the full aperture spectrum. Figure 9 shows the continuum subtracted SH spectra with a LTE water model overplotted for two of the embedded sources. The observed emission features are similar to those seen in the more evolved disks around T Tauri stars by Salyk et al. (2008); Carr & Najita (2008).

To derive basic excitation parameters the full IRS SH spectra are compared with single temperature LTE models using the HITRAN 2004 database (Rothman et al. 2005). The model assumes a single slab of gas of solid angle (Ω), temperature (T), column density (N) and intrinsic linewidth (b). Without exception the derived excitation temperatures are high, $T_{\text{ex}} = 700 - 1500$ K. Best fits are achieved for models with large H_2O column densities, $N \gtrsim 10^{17} \text{ cm}^{-2}$, and small emission regions, $r \lesssim \text{few AU}$, comparable to what is found for the T Tauri stars observed by Salyk et al. (2008); Carr & Najita (2008). An accurate and fully constrained fit is not possible with the low ($R = 600$) resolution SH spectra. It may be possible to extract more information through non-LTE models (see Meijerink et al. 2009) but such models are outside the scope of this paper.

For C_2H_2 , HCN and CO_2 none of the spectra have sufficient S/N to derive reliable excitation temperatures and column den-

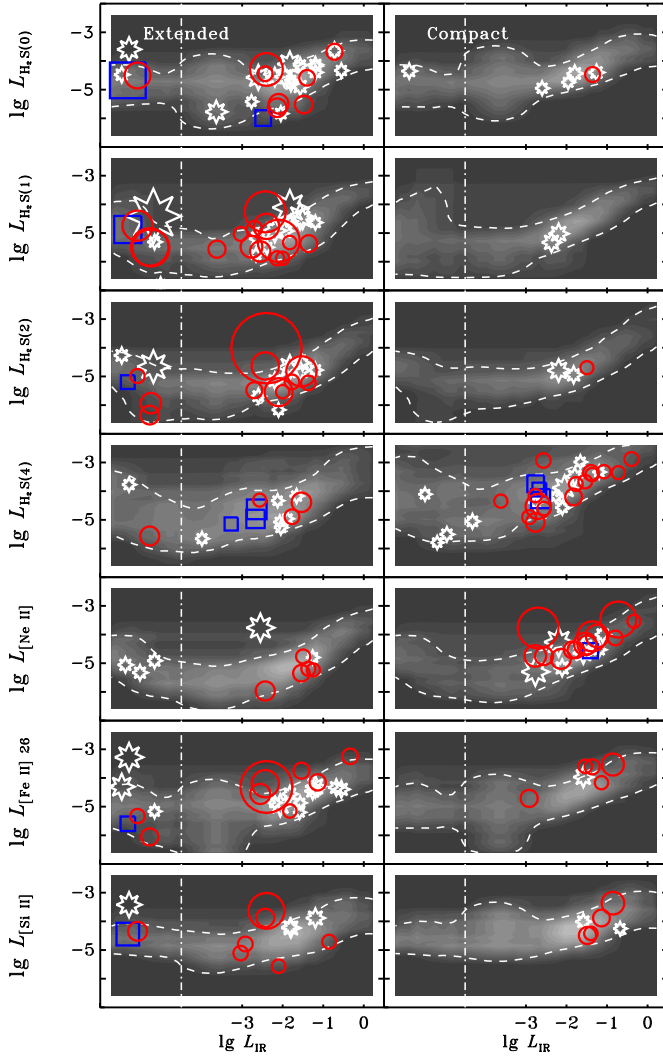


Fig. 5. Line luminosities and upper limits (in solar luminosity) as functions of the mid-IR luminosity (calculated from the IRS spectra) for the estimated extended and compact source contributions to the total line strength. The red circles show the truly embedded sources, white stars the disk sources (this paper and Lahuis et al. 2007b) and blue squares the unclassified sources. Shown are all 4σ line detections, the symbol size scales with line error. The observed upper limits listed in Tables 3 and 4 are shown as grayscale images with dashed contours. The upper limits are presented as number density distributions with the contours bracketing the 10 and 90 % ranges. All sources plotted left of the vertical dashed line either have no detected continuum in the IRS spectra or the spectrum does not cover the mid-IR range (x-position offset for clarity).

sities or even solid detections. High spatial and/or spectral resolution observations are required to further constrain the model parameters. The importance of high resolution data is illustrated in Salyk et al. (2008) who obtained high resolution $3\mu\text{m}$ spectra for two disk sources, AS 205A and DR Tau, following the initial detection of hot H_2O emission in the *Spitzer*-IRS SH spectra. We therefore do not list fit parameters for individual sources but limit ourselves to summarizing detections in Table 2.

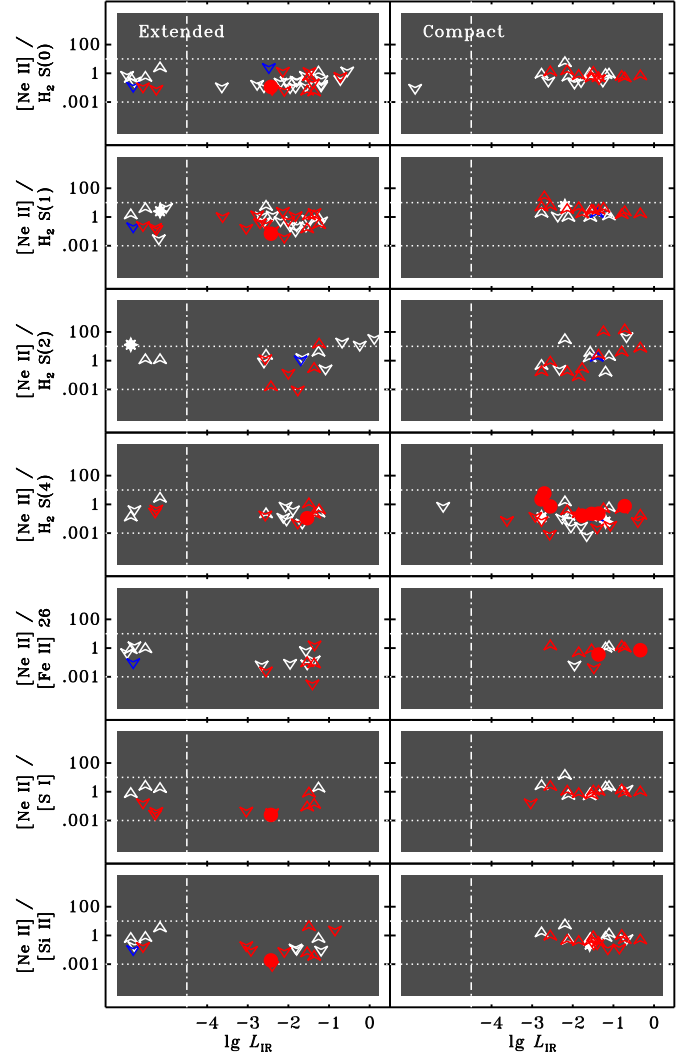


Fig. 6. Line ratios (filled symbols) and line ratio upper and lower limits of [Ne II] with a number of H_2 and atomic lines. The use of symbols and colors is the same as in Figure 5. All sources plotted left of the vertical dashed line either have no detected continuum in the IRS spectra or the spectrum does not cover the mid-IR range (x-position offset for clarity). The two horizontal dotted lines span the range of 0.001 to 10 within which most detections fall. This range is also indicated in Figure 10 which shows [Ne II] line ratios from shock models by Hollenbach & McKee (1989). Note that most line ratios displayed here are upper and lower limits. Only for [Ne II]/ H_2 S(4) a reasonable number of line ratios (filled red circles) exist.

4.4. Correlations and line ratios

Figure 5 shows the observed line luminosities (for all 4σ detections) as function of the mid-IR ($12.8 - 15.5\mu\text{m}$) continuum luminosities as calculated from the *Spitzer*-IRS spectra. The mid-IR continuum luminosity is used as a qualitative measure of the hot-dust component.

Both the line strengths and the upper limits fall in a narrow band, ~ 2 orders of magnitude, spanning the full L_{IR} range. All species show a positive trend with L_{IR} , which is most clearly observed in the compact H_2 S(4) and [Ne II] line emission. As discussed above, the presence of weaker line emission than cur-

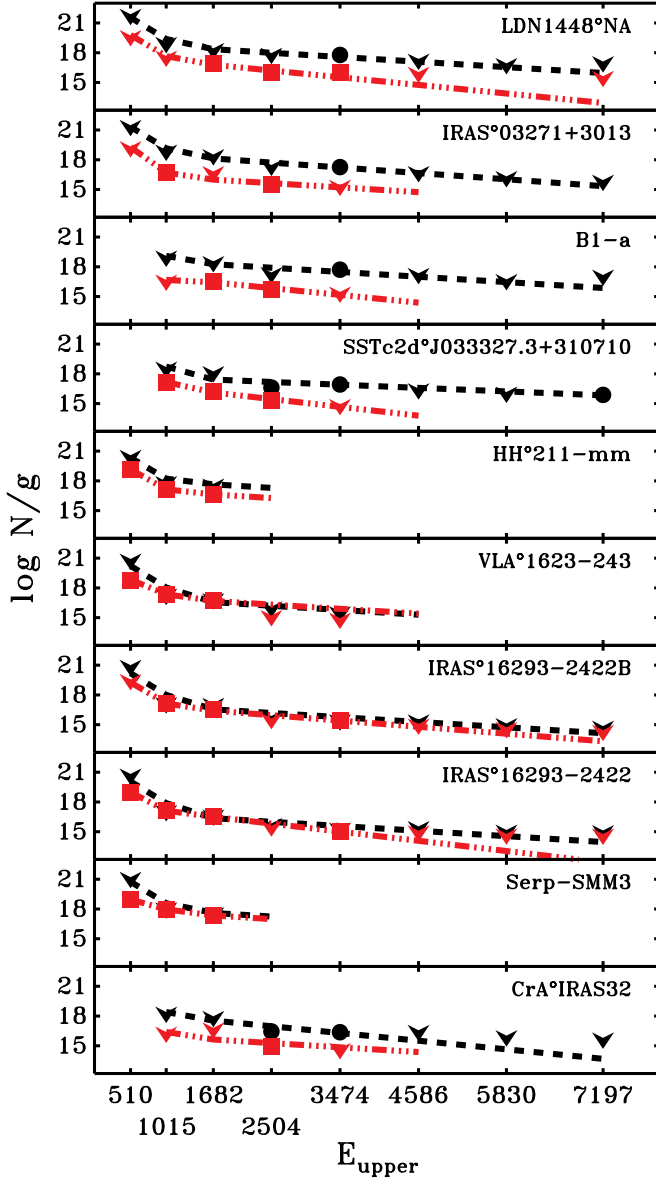


Fig. 7. Excitation diagrams of the observed H_2 emission. Plotted with black circles is the observed spatially compact emission and with red squares the spatially extended emission. The arrows are the derived upper limits. Overplotted with respectively dashed and dashed/dotted lines is a two temperature fit to the observed H_2 emission, as seen by the difference in slope going from the low to the high energy states. The inferred temperatures are listed in Table 5. Note that the low temperature component is not always well constrained.

rently observed cannot be excluded. However, the current dataset does exclude strong line emission for the weak IR sources.

Figure 6 shows the line ratios and line ratio limits of $[\text{Ne II}]$ with a number of H_2 and atomic lines. All ratios fall within a range of a few orders of magnitudes and show no obvious trends. The line ratio limits do not reveal any sources deviating from this, consistent with the fact that the observed line luminosities are close to the line luminosity upper limits as shown in Figure 5. Higher resolution and high sensitivity observations (e.g. with

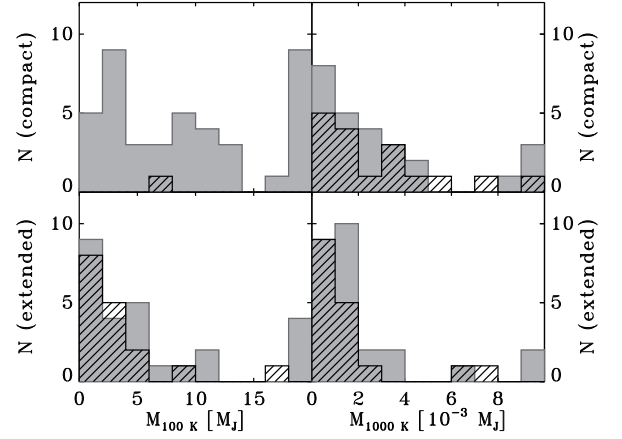


Fig. 8. Distribution of H_2 masses (in Jupiter mass) for both the compact and the extended component assuming $T_{\text{ex}} = 100$ and 1000 K. The gray bars represent upper limits on the gas mass, while the hatched bars indicate sources where H_2 is detected at 4σ or more. For 100 K this includes sources with the H_2 S(0) and/or S(1) line detected and for 1000 K sources with any of the higher J lines detected. The highest bar also includes all sources with masses higher than the upper plot limit.

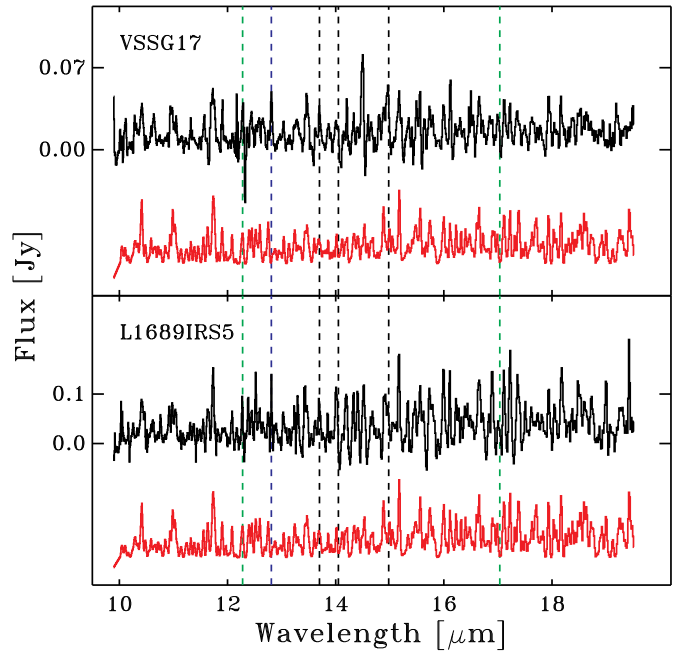


Fig. 9. Molecular emission toward two truly embedded sources. Plotted for each source are the continuum subtracted *Spitzer* IRS-SH spectra (top spectrum in black) and a single temperature LTE water model at $T_{\text{ex}} = 900$ K (bottom spectrum in red). Vertical lines indicate the positions of a few important spectral features; from left to right H_2 S(2), $[\text{Ne II}]$, C_2H_2 , HCN , CO_2 and H_2 S(1). In VSSG17 CO_2 and tentative C_2H_2 and HCN emission can be seen.

the MIRI instrument aboard the James Webb Space Telescope) will be required to overcome this limitation.

5. Discussion

5.1. General trends

Atomic fine structure lines, H_2 pure rotational lines and molecular emission features are observed toward the majority of the sources in our sample, both as compact and extended emission. Table 2 presents a qualitative overview of the identified emission. The compact emission is dominated by $[\text{Ne II}]$, high- J H_2 emission lines and hot H_2O emission. The extended emission is dominated by low- J H_2 emission lines. A small number of sources show line emission from both the extended and compact components at the same time. H_2O emission is seen in the compact component toward both compact and extended emission dominated sources.

The increase of the line strength with increasing mid-IR luminosity suggests that the heating mechanism of the dust and the excitation of the line may have the same physical origin. Besides heating due to the protostellar luminosity, UV radiation from the star-disk accretion boundary layer escaping through the outflow cones may heat both the dust and the gas (see §5.3).

A global comparison in Figures 5 and 6 between the truly embedded sources and the disk sample of (Lahuis et al. 2007b) shows that both samples exhibit spatially compact and extended emission at the same time. Both samples also show compact hot water emission. The main difference is in the statistics of the extended emission. While in the compact emission the difference between the two samples is small (e.g. hot water emission is observed toward $\sim 40\%$ of the disk sources and $\sim 30\%$ of the truly embedded sources) the difference is large for the extended component. Extended emission is observed toward $\sim 1/3$ of the disk sources and $\sim 2/3$ of the truly embedded sources. The extended emission observed toward the disk sources represents the PDR emission from the local environment, in particular the extended PDR in ρ Oph. Therefore it is fair to assume that a significant fraction of the extended emission observed toward the truly embedded sources has its origin from the source and not from the environment.

Because the *Spitzer*-IRS spectral and spatial resolution is moderate, the level to which we can qualitatively and quantitatively constrain the excitation and the physical environment of young stars is limited. High spatial and/or high spectral resolution observations are required to separate the different emission components either through direct observations or by spectral decomposition. A prime example of this is the study of $[\text{Ne II}]$ emission toward stage II disk sources. The initial *Spitzer* detections of compact $[\text{Ne II}]$ emission (Lahuis et al. 2007b; Pascucci et al. 2007) raised excitement and suggested a possible disk surface origin of the $[\text{Ne II}]$ emission which was supported by model results from Glassgold et al. (2007). However, recent high resolution ground based observations (Herczeg et al. 2007; Pascucci & Sterzik 2009; van Boekel et al. 2009) have shown that high resolution follow-up observations are essential for a proper interpretation. Pascucci & Sterzik (2009) and van Boekel et al. (2009) argue for an outflow/jet origin of the spatially unresolved *Spitzer* $[\text{Ne II}]$ emission observed toward T Tau, Sz102 and VW Cha. Recent model results (Hollenbach & Gorti 2009) confirm that observable $[\text{Ne II}]$ emission may be produced through X-ray and FUV irradiation of the proto-planetary disk surface and through internal shocks in protostellar winds. This is confirmed by Güdel et al. (2010) where disk and jet contributions are separated through a statistical analysis of $[\text{Ne II}]$ emission of a large sample of *Spitzer* sources.

Although a detailed analysis of individual sources may not be possible, general conclusions may be drawn. By

looking at the overall line fluxes and line ratios observed (see Figures 5 and 6) we can draw general conclusions about the protostellar environment. In the following sections we will therefore compare the observations with published shock and PDR models and discuss possible origins of the observed emission.

5.2. Shock excitation

Many of the observed emission lines, including $[\text{Ne II}]$, $[\text{Fe II}]$, $[\text{Si I}]$ and $[\text{Si II}]$ are predicted to be strong in J -type shocks (Hollenbach & McKee 1989) with the main exception being the low- J H_2 lines. The hot (~ 1500 K) H_2 emission observed, in particular, is expected in the cooling post-shock gas (e.g. van den Ancker et al. 1999). The observed strengths of the atomic emission lines are comparable with predictions by shock models, but the observed line ratios are not sufficiently constrained to draw any conclusions about precise shock velocities. However for $[\text{Ne II}]$ to be strong, shock velocities in excess of $\sim 70 \text{ km s}^{-1}$ are required. Figure 10 shows that the range of line ratios predicted by the models is consistent with those observed (Figure 6) over a range of expected pre-shock densities and shock velocities.

The $\text{H}_2 \text{S}(0)$ line is predicted to be the weakest J -shock feature in Hollenbach & McKee (1989). The observed line ratios and upper limits of the $[\text{Ne II}]/\text{H}_2 \text{S}(0)$ line ratio for the extended component in the disk sources (Lahuis et al. 2007b) is ≤ 1 (see Figure 6). In J -shock models the $[\text{Ne II}]/\text{H}_2 \text{S}(0)$ ratio is up to two orders of magnitude higher (see Figure 10). We therefore exclude J -shocks as the origin for the extended low- J warm H_2 emission toward the embedded and disk sources. The extended $[\text{Fe II}]$ emission observed toward the disk sources may have a similar origin as the warm H_2 emission though this cannot be constrained by the J -shock models itself.

In non-dissociative C -shocks low- J H_2 emission is strong (Kaufman & Neufeld 1996) and the observed strengths of the H_2 lines are consistent with C -shock model predictions. At the same time atomic lines are not expected to be strong. The low- J H_2 lines, mostly observed in the spatially extended component, may partly have a C -shock origin in material entrained by the outflow. However given that $[\text{Fe II}]$ is also observed as extended emission, C -shocks are not likely to be the sole origin of the extended line emission.

5.3. PDR models

Models of photodissociation regions (PDRs) predict line strengths for the low- J H_2 , $[\text{Fe II}]$ and $[\text{Si II}]$ emission comparable to the observed line strengths for $n \sim 10^2 - 10^5 \text{ cm}^{-3}$ and a radiation field of $\sim 10^1 - 10^3 G_0$ (Hollenbach et al. 1991; Kaufman et al. 2006). These values are consistent with those estimated for the outer envelope. The H_2 excitation temperatures of $\sim 350 - 700$ K (see Figure 7) are comparable with gas surface temperatures for PDRs with the range of densities and radiation fields mentioned above (Kaufman et al. 1999, and the PDRT⁴).

A PDR origin of the observed extended emission therefore appears to be plausible. It is likely that the observed emission originates in the PDR tracing the surfaces of the extended outflow cavity for the embedded sources, although there may also be a contribution from extended lower density cloud material in the beam for some sources, especially in Ophiuchus. Weak C -shocks may be present as well (see Section 5.2). The pres-

⁴ Photo Dissociation Region Toolbox
<http://dustem.astro.umd.edu/pdrt/>

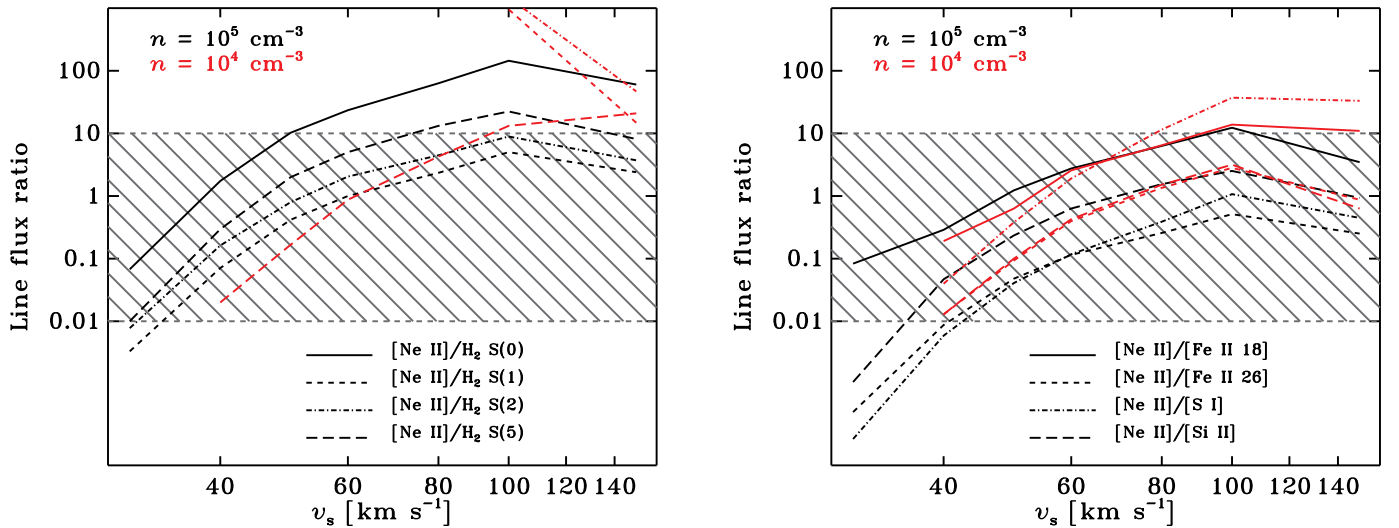


Fig. 10. [Ne II] line ratios from *J*-shock models by Hollenbach & McKee (1989) for pre-shock densities of 10^5 (black) and 10^4 (red). Note that for the low density case the [Ne II] ratios with the low-*J* H₂ lines are large and quickly fall off the plot. The hatched area indicates the range of observed line ratios (see Figure 6).

ence of extended photon-heated gas along outflow cavities has recently also been inferred from narrow high-*J* CO submillimeter emission lines (van Kempen et al. 2009b,a; Spaans et al. 1995) and has also been suggested based on ISO-LWS atomic fine-structure line data (Molinari et al. 2001). Although the [S I] emission is almost exclusively observed in the extended component, [S I] is not strong in PDR models. At the warm PDR surfaces most sulfur will be in the form of S⁺.

The origin of the exciting UV radiation field is still under debate (see §1). Suggested origins are UV photons: i) escaping from the star-disk boundary layer near the central protostar (Spaans et al. 1995), and ii) from high-velocity shocks directly associated with the more extended jets and outflows (Neufeld & Dalgarno 1989; Molinari et al. 2001). In both cases, the UV field consists of a continuous spectrum with possibly some discrete lines due to recombining atoms superposed. In our sample we observe sources simultaneously exhibiting signatures of extended PDR/C-shock and compact *J*-shock emission and sources showing only extended PDR/C-shock emission and no compact shock emission (see Table 2), thus leaving all options open.

In order to advance on the current situation it will be important to get multiple, when possible spatially and/or spectrally resolved, detections per source on key lines such as [Ne II], [S I], [O I] 63.2 μ m, [C II] 157.7 μ m and the low-*J* H₂ lines. [Ne II] and [S I] are clear indicators of *J*-shocks, whereas the [O I]/[C II] ratio and the absence or presence of [Si II] and [Fe II] help to distinguish and characterize PDR and C-shock emission. In his PhD thesis van den Ancker (1999, Chapter 10) presents a useful summary of the relevant issues. High velocity resolution [Ne II] observations are possible from the ground although the lines presented here are not strong enough for current instrumentation. JWST will provide an inventory of the key mid-IR emission lines towards a large sample of embedded sources. *Herschel* will provide the possibility to observe highly-excited CO, [O I] and [C II] and provide high velocity resolution observations for some far-IR lines through HIFI.

5.4. Molecular emission and absorption

While molecular emission is seen toward a number of sources, none of the truly embedded sources show absorption bands of HCN, C₂H₂ and/or CO₂. This in contrast with high and intermediate mass stars (Lahuis & van Dishoeck 2000; Boonman et al. 2003; Boonman & van Dishoeck 2003, Thi et al. in prep.) where these molecules are characteristic of hot-core chemistry (Doty et al. 2002; Rodgers & Charnley 2003). Toward ULIRGs absorption of C₂H₂, HCN and CO₂ has been observed by Lahuis et al. (2007a) suggesting the presence of pressure confined massive star formation. The absence of signatures of C₂H₂ and HCN absorption towards the low-mass sources in our sample is not surprising, however. To produce absorption features observable with IRS one needs both high column densities, requiring orders of magnitude enhancement of the molecular abundances compared with the normal cloud abundances, and a strong infrared background. These conditions are met in the inner envelope around higher-mass stars during the hot-core phase (Lahuis & van Dishoeck 2000), but for solar-mass stars the inner envelope regions do not become hot enough ($T > 300$ K) to produce the required chemical enrichment. Only in the inner regions of protoplanetary disk are these conditions met and absorption features have only been observed with *Spitzer* and near-IR ground-based instruments (Lahuis et al. 2006; Gibb et al. 2007) under a favorable, near edge-on, source alignment toward two sources (IRS 46 and GV Tau).

Molecular emission from H₂O is observed in a quarter of the truly embedded sources in our sample and emission from C₂H₂, HCN and CO₂ is tentatively observed in a few sources. What is the origin of this emission: the young disk or outflow?

Mid-infrared H₂O and OH emission is observed to be associated with outflows such as HH 211, where prominent lines are detected at the bow shock position offset from the protostar itself (Tappe et al. 2008, e.g.). Emission features of C₂H₂, HCN and CO₂ seen toward Cepheus A East are evidence of gas-phase abundance enhancements through sputtering of icy grain mantles in shocked regions (Sonnentrucker et al. 2006, 2007). Since our data show neither the high-*J* OH lines nor prominent C₂H₂,

HCN or CO₂ emission, these scenarios do not appear to explain our data.

Strong H₂O mid-infrared emission has also been observed with *Spitzer* toward the stage 0 source (NGC1333-IRAS4B by Watson et al. 2007) and attributed to disk accretion shocks, but it is unclear whether this interpretation is unique and how general this phenomenon is (see also Jørgensen & van Dishoeck 2010). None of the other stage 0 sources in our sample (in particular VLA_1623-243, IRAS_16293-2422, IRAS_16293-2422B, Serp-S68N, Serp-SMM3 and Serp-SMM4) show hot H₂O emission. One Stage I source, GSS30-IRS1, exhibits strong CO mid-infrared lines indicative of accretion shocks (Pontoppidan et al. 2002) but does not show any H₂O lines in our *Spitzer* data.

On the other hand, strong H₂O, C₂H₂, HCN, CO₂ and/or OH lines have clearly been detected from a number of more evolved stage II sources arising from the inner AU of the disk (Carr & Najita 2008; Salyk et al. 2008). The molecular emission observed toward the embedded sources in our sample has characteristics similar to those observed toward these disk sources: high T_{ex} , high n and a small size of the emitting region. In particular, T_{ex} is significantly higher than the value of ~ 170 K observed toward NGC 1333 IRAS4B (Watson et al. 2007). It is therefore plausible that the molecular emission observed in our sample also has its origin in the inner AU of the young disks. In other words, we may be looking through a window onto the embedded young disks (see e.g. Cernicharo et al. 2000).

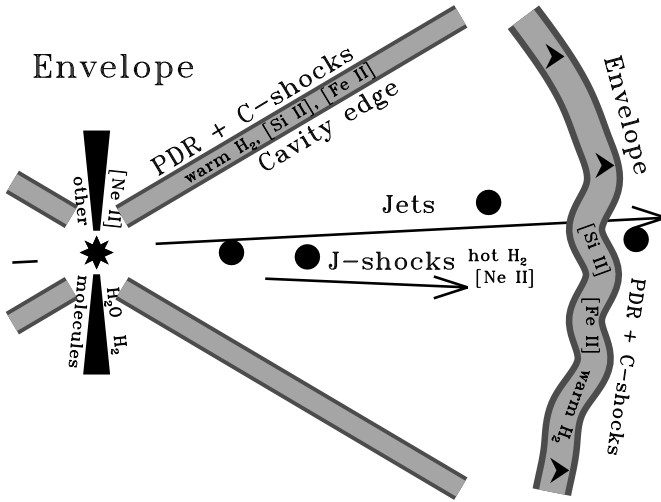


Fig. 11. Cartoon image to illustrate the various emission components for the embedded sources as seen by mid-IR *Spitzer*-IRS observations. Extended emission may be observed as PDR and/or C-shock emission from the irradiated and accelerated gas in the cavity and envelope surfaces. Compact J-shock emission can be observed from shocks within high-velocity jets, indicated by filled circles. Disk emission may be observed for systems viewed along the outflow cavity.

5.5. Source environment

The general picture which emerges is that of a young star surrounded by a forming disk embedded in the natal envelope. Winds and jets from the young star produce holes and cavities in the envelope. Within the jets and in its boundary regions with the envelope, supersonic shock waves are produced which locally compress and heat the gas producing, among others, hot

H₂ and [Ne II] emission. Non-dissociative C-shocks in material entrained by the extended outflow produce warm spatially extended H₂ emission. C-shocks are however not the sole origin of the observed extended emission: the presence of spatially extended [Fe II] and [Si II] emission argues against this and points to the presence of extended PDRs. UV radiation produced by the young star system heat the cavity walls and envelope surface creating extended PDR regions. Emission from the young disk, in particular that from molecules such as H₂O, can be observed directly by looking along the outflow cavities and/or through a patchy envelope.

Spatially extended PDR and C-shock emission is observed toward $\sim 2/3$ of the sources, including the stage 0 sources. Some of this emission may come from the local environment, as observed toward the disk sources. Extended emission is observed toward $\sim 1/3$ of the disk sources. Therefore a significant fraction of the extended emission observed toward the embedded sources may originate from the sources themselves. This is consistent with most sources having a sizeable outflow cavity. The outflow cavities are most easily observed toward sources where the outflow is seen face-on or at moderate inclination angles. Toward systems seen at large inclination angles the extinction through the envelope will prohibit detecting the emission from the outflow cavity walls, though this will depend on the observed wavelength of the emission and its location within the cavity emission. Thus, given a uniform line-of-sight distribution, extended emission from the outflow cavity walls should be observed toward a large fraction of the sources. This is the case in our sample of embedded sources.

The presence of hot H₂O emission suggests a strong similarity between the embedded stage-I disks and the more evolved stage-II disks. None of the known stage-0 sources in our sample show signs of hot H₂O emission, implying that their disks have either different characteristics or are much more obscured.

Figure 11 shows a graphical representation of the picture described above displaying the different components and the location of the observed emission. In this picture, the main difference with the more evolved stage II disks is that the latter sources lack the extended emission from PDR and C-shocks along the cavity edge. The limitations of the *Spitzer*-IRS data (low spatial and spectral resolution) prohibit us from making conclusive statements on individual sources.

6. Conclusions

A survey of the mid-infrared gas phase pure rotational lines of molecular hydrogen and a number of atomic fine structure transitions has been carried out toward a sample of 61 class I sources with the *Spitzer*-IRS of which 43 are truly embedded protostars. Both extended and compact source emission has been detected toward a majority of the sources. Compact emission, most prominently seen in hot H₂, [Ne II] and H₂O lines, is seen toward $\sim 1/4$ to $1/3$ of the truly embedded sources. The compact hot H₂ and [Ne II] emission is believed to have its origin predominantly in dissociative J-shocks in the outflow jets, though a true disk component may be present. The H₂O emission is consistent with an origin in the inner regions of the young protostellar disk, similar to the H₂O emission from the more evolved systems. Extended emission, dominated by low-J H₂ and [Fe II] emission, is observed toward $\sim 2/3$ of the truly embedded sources, both stage 0 and I sources. The extended emission is thought to originate from PDRs along the outflow cavity walls with possible contributions from non-dissociative C-shocks.

These observations have shown the capability of *Spitzer* to observe the gas around young stars. It clearly shows emission from PDR and shock excited gas by the presence of various H_2 and atomic lines. However, its limited spatial and spectral resolution prevents a quantitative analysis of the excitation conditions.

Sources with atomic fine structure line emission, H_2 and H_2O emission are excellent candidates for follow up with various ground based instruments and near-IR and far-IR space-based instruments on *Herschel* and JWST. The major far-IR cooling lines of $[\text{O I}]$ and $[\text{C II}]$ as well as high- J CO observable with *Herschel* can provide important excitation constraints (van Kempen et al. 2010). Several of the sources in this sample are targets in the “Water in Star-forming regions with *Herschel*” (WISH) and “Dust, Ice and Gas in Time” (DIGIT) *Herschel* key programs. Future mid-IR observations with JWST-MIRI will allow the detection of weak emission lines and provide many more diagnostics to separate the physical processes. Such high spectral and spatial resolution observations are essential to constrain the location and extent of the emission (either by direct detection or through velocity resolved spectra) to properly understand the physical environment around the young stars.

The spectra of the compact component of the truly embedded sources show remarkable similarities with those of the evolved disk sources, both in terms of absolute fluxes and flux ratios. Both characteristic J -shock emission, hot H_2 and $[\text{Ne II}]$, and true disk emission through the molecular emission lines are observed. In particular, the molecular emission may offer a unique tool to study the young forming disks in their earliest phases and compare these with the more evolved stage II disks.

Acknowledgements. Astrochemistry in Leiden is supported by a NWO Spinoza grant and a NOVA grant. Support for this work, part of the *Spitzer* Legacy Science Program, was provided by NASA through contract 1224608 issued by the Jet Propulsion Laboratory, California Institute of Technology, under NASA contracts 1407, 1256316, and 1230779. We thank the referee, David Hollenbach, for his thorough and constructive review which helped to improve our paper. All members of the c2d-IRS team are thanked for their feedback; detailed comments from Klaus Pontoppidan are particularly appreciated. We thank the Lorentz Center in Leiden for hosting several meetings that contributed to this paper. Lars Kristensen and Tim van Kempen helped to identify the evolutionary stages of some sources.

References

- Bally, J., Reipurth, B., & Davis, C. J. 2007, in *Protostars and Planets V*, ed. B. Reipurth, D. Jewitt, & K. Keil, 215–230
- Bergin, E. A. 2009, ArXiv e-prints
- Bergin, E. A., Aikawa, Y., Blake, G. A., & van Dishoeck, E. F. 2007, *Protostars and Planets V*, 751
- Blake, G. A. & Boogert, A. C. A. 2004, *ApJ*, 606, L73
- Boersma, C., Bouwman, J., Lahuis, F., et al. 2008, ArXiv e-prints, 804
- Boogert, A. C. A., Pontoppidan, K. M., Knez, C., et al. 2008, *ApJ*, 678, 985
- Boonman, A. M. S. & van Dishoeck, E. F. 2003, *A&A*, 403, 1003
- Boonman, A. M. S., van Dishoeck, E. F., Lahuis, F., & Doty, S. D. 2003, *A&A*, 399, 1063
- Bruderer, S., Benz, A. O., Bourke, T. L., & Doty, S. D. 2009a, *A&A*, 503, L13
- Bruderer, S., Benz, A. O., Doty, S. D., van Dishoeck, E. F., & Bourke, T. L. 2009b, *ApJ*, 700, 872
- Carr, J. S. & Najita, J. R. 2008, *Science*, 319, 1504
- Cassen, P. & Moosman, A. 1981, *Icarus*, 48, 353
- Cernicharo, J., Noriega-Crespo, A., Cesarsky, D., et al. 2000, *Science*, 288, 649
- Chiang, H., Looney, L. W., Tassis, K., Mundy, L. G., & Mouschovias, T. C. 2008, *ApJ*, 680, 474
- Comerón, F. 2008, *The Lupus Clouds (ASP Conf. Ser.)*, 295–
- Crapsi, A., van Dishoeck, E. F., Hogerheijde, M. R., Pontoppidan, K. M., & Dullemond, C. P. 2008, *A&A*, 486, 245
- de Geus, E. J., de Zeeuw, P. T., & Lub, J. 1989, *A&A*, 216, 44
- de Graauw, T., Haser, L. N., Beintema, D. A., et al. 1996, *A&A*, 315, L49
- Decin, L., Morris, P. W., Appleton, P. N., et al. 2004, *ApJS*, 154, 408
- Doty, S. D., van Dishoeck, E. F., van der Tak, F. F. S., & Boonman, A. M. S. 2002, *A&A*, 389, 446
- Draine, B. T. & McKee, C. F. 1993, *ARA&A*, 31, 373
- Enoch, M. L., Young, K. E., Glenn, J., et al. 2006, *ApJ*, 638, 293
- Espaillat, C., Calvet, N., D’Alessio, P., et al. 2007, *ApJ*, 664, L111
- Evans, N. J., Dunham, M. M., Jørgensen, J. K., et al. 2009, *ApJS*, 181, 321
- Evans, II, N. J., Allen, L. E., Blake, G. A., et al. 2003, *PASP*, 115, 965
- Geers, V. C., Augereau, J.-C., Pontoppidan, K. M., et al. 2006, *A&A*, 459, 545
- Gibb, E. L., Van Brunt, K. A., Brittain, S. D., & Rettig, T. W. 2007, *ApJ*, 660, 1572
- Glassgold, A. E., Najita, J. R., & Igea, J. 2007, *ApJ*, 656, 515
- Gorti, U. & Hollenbach, D. 2008, *ApJ*, 683, 287
- Güdel, M., Lahuis, F., Briggs, K. R., et al. 2010, *A&A*, submitted
- Habart, E., Walmsley, M., Verstraete, L., et al. 2005, *Space Science Reviews*, 119, 71
- Harvey, P. M., Chapman, N., Lai, S.-P., et al. 2006, *ApJ*, 644, 307
- Herczeg, G. J., Najita, J. R., Hillenbrand, L. A., & Pascucci, I. 2007, *ApJ*, 670, 509
- Hollenbach, D. 1997, in *IAU Symp. 182: Herbig-Haro Flows and the Birth of Stars*, ed. B. Reipurth & C. Bertout, 181
- Hollenbach, D. & Gorti, U. 2009, *ApJ*, 703, 1203
- Hollenbach, D. & McKee, C. F. 1989, *ApJ*, 342, 306
- Hollenbach, D. J., Takahashi, T., & Tielens, A. G. G. M. 1991, *ApJ*, 377, 192
- Hollenbach, D. J. & Tielens, A. G. G. M. 1999, *Reviews of Modern Physics*, 71, 173
- Houck, J. R., Roellig, T. L., van Cleve, J., et al. 2004, *ApJS*, 154, 18
- Jørgensen, J. K., Lahuis, F., Schöier, F. L., et al. 2005, *ApJ*, 631, L77
- Jørgensen, J. K., Schöier, F. L., & van Dishoeck, E. F. 2002, *A&A*, 389, 908
- Jørgensen, J. K. & van Dishoeck, E. F. 2010, *ApJ*, 710, L72
- Jørgensen, J. K., van Dishoeck, E. F., Visser, R., et al. 2009, *A&A*, 507, 861
- Kaufman, M. J. 1995, PhD thesis, The Johns Hopkins University
- Kaufman, M. J. & Neufeld, D. A. 1996, *ApJ*, 456, 611
- Kaufman, M. J., Wolfire, M. G., & Hollenbach, D. J. 2006, *ApJ*, 644, 283
- Kaufman, M. J., Wolfire, M. G., Hollenbach, D. J., & Luhman, M. L. 1999, *ApJ*, 527, 795
- Keene, J. & Masson, C. R. 1990, *ApJ*, 355, 635
- Kenyon, S. J., Dobrzycka, D., & Hartmann, L. 1994, *AJ*, 108, 1872
- Lahuis, F. 2007, PhD thesis, Leiden Observatory, Leiden University, P.O. Box 9513, 2300 RA Leiden, The Netherlands
- Lahuis, F. & Boogert, A. 2003, in *SFCHEM 2002: Chemistry as a Diagnostic of Star Formation*, ed. C. L. Curry & M. Fich, 335
- Lahuis, F., Spoon, H. W. W., Tielens, A. G. G. M., et al. 2007a, ArXiv Astrophysics e-prints
- Lahuis, F. & van Dishoeck, E. F. 2000, *A&A*, 355, 699
- Lahuis, F., van Dishoeck, E. F., Blake, G. A., et al. 2007b, *ApJ*, 665, 492
- Lahuis, F., van Dishoeck, E. F., Boogert, A. C. A., et al. 2006, *ApJ*, 636, L145
- Lommen, D., Jørgensen, J. K., van Dishoeck, E. F., & Crapsi, A. 2008, *A&A*, 481, 141
- Meijerink, R., Glassgold, A. E., & Najita, J. R. 2008, *ApJ*, 676, 518
- Meijerink, R., Pontoppidan, K. M., Blake, G. A., Poelman, D. R., & Dullemond, C. P. 2009, *ApJ*, 704, 1471
- Meyer, M. R. & the entire FEPS team. 2007, *PASP*, 118, 1690
- Molinari, S., Noriega-Crespo, A., & Spinoglio, L. 2001, *ApJ*, 547, 292
- Najita, J., Carr, J. S., & Mathieu, R. D. 2003, *ApJ*, 589, 931
- Neufeld, D. A. & Dalgarno, A. 1989, *ApJ*, 340, 869
- Neufeld, D. A. & Kaufman, M. J. 1993, *ApJ*, 418, 263
- Neufeld, D. A., Nisini, B., Giannini, T., et al. 2009, *ApJ*, 706, 170
- Noriega-Crespo, A., Morris, P., Marleau, F. R., et al. 2004, *ApJS*, 154, 352
- Öberg, K. I., Boogert, A. C. A., Pontoppidan, K. M., et al. 2008, *ApJ*, 678, 1032
- Pascucci, I., Gorti, U., Hollenbach, D., et al. 2006, *ApJ*, 651, 1177
- Pascucci, I., Hollenbach, D., Najita, J., et al. 2007, *ApJ*, 663, 383
- Pascucci, I. & Sterzik, M. 2009, *ApJ*, 702, 724
- Pontoppidan, K. M., Boogert, A. C. A., Fraser, H. J., et al. 2008, *ApJ*, 678, 1005
- Pontoppidan, K. M., Dullemond, C. P., van Dishoeck, E. F., et al. 2005, *ApJ*, 622, 463
- Pontoppidan, K. M., Schöier, F. L., van Dishoeck, E. F., & Dartois, E. 2002, *A&A*, 393, 585
- Ray, T., Dougados, C., Bacciotti, F., Eisloffel, J., & Chrysostomou, A. 2007, in *Protostars and Planets V*, ed. B. Reipurth, D. Jewitt, & K. Keil, 231–244
- Robitaille, T. P., Whitney, B. A., Indebetouw, R., Wood, K., & Denzmore, P. 2006, *ApJS*, 167, 256
- Rodgers, S. D. & Charnley, S. B. 2003, *ApJ*, 585, 355
- Rothman, L. S., Jacquemart, D., Barbe, A., et al. 2005, *Journal of Quantitative Spectroscopy and Radiative Transfer*, 96, 139
- Salyk, C., Pontoppidan, K. M., Blake, G. A., et al. 2008, *ApJ*, 676, L49
- Shang, H., Li, Z.-Y., & Hirano, N. 2007, in *Protostars and Planets V*, ed. B. Reipurth, D. Jewitt, & K. Keil, 261–276
- Sonnentrucker, P., González-Alfonso, E., & Neufeld, D. A. 2007, *ApJ*, 671, L37

- Sonnentrucker, P., González-Alfonso, E., Neufeld, D. A., et al. 2006, *ApJ*, 650, L71
- Spaans, M., Hogerheijde, M. R., Mundy, L. G., & van Dishoeck, E. F. 1995, *ApJ*, 455, L167+
- Stäuber, P., Doty, S. D., van Dishoeck, E. F., Jørgensen, J. K., & Benz, A. O. 2004, *A&A*, 425, 577
- Sternberg, A. & Neufeld, D. A. 1999, *ApJ*, 516, 371
- Straizys, V., Cernis, K., & Bartasiute, S. 1996, *Baltic Astronomy*, 5, 125
- Tappe, A., Lada, C. J., Black, J. H., & Muench, A. A. 2008, *ApJ*, 680, L117
- Terebey, S., Shu, F. H., & Cassen, P. 1984, *ApJ*, 286, 529
- Thi, W. F., van Dishoeck, E. F., Blake, G. A., et al. 2001, *ApJ*, 561, 1074
- Tielens, A. G. G. M. & Hollenbach, D. 1985a, *ApJ*, 291, 747
- Tielens, A. G. G. M. & Hollenbach, D. 1985b, *ApJ*, 291, 722
- Tobin, J. J., Hartmann, L., Looney, L. W., & Chiang, H. 2010, *ApJ*, 712, 1010
- van Boekel, R., Güdel, M., Henning, T., Lahuis, F., & Pantin, E. 2009, *A&A*, 497, 137
- van den Ancker, M. 1999, PhD thesis, University of Amsterdam
- van den Ancker, M. E., Wesselius, P. R., Tielens, A. G. G. M., van Dishoeck, E. F., & Spinoglio, L. 1999, *A&A*, 348, 877
- van Dishoeck, E. F. 2004, *ARA&A*, 42, 119
- van Kempen, T. A., Green, J. D., Evans, N. J., et al. 2010, *A&A*, ArXiv 1005.2548
- van Kempen, T. A., van Dishoeck, E. F., Güsten, R., et al. 2009a, *A&A*, 507, 1425
- van Kempen, T. A., van Dishoeck, E. F., Güsten, R., et al. 2009b, *A&A*, 501, 633
- van Kempen, T. A., van Dishoeck, E. F., Salter, D. M., et al. 2009c, *A&A*, 498, 167
- Velusamy, T., Langer, W. D., & Marsh, K. A. 2007, *ApJ*, 668, L159
- Walmsley, M., Des Forêts, G. P., & Flower, D. 2005, in *IAU Symposium*, ed. D. C. Lis, G. A. Blake, & E. Herbst, 135
- Watson, D. M., Bohac, C. J., Hull, C., et al. 2007, *Nature*, 448, 1026
- Werner, M. W., Roellig, T. L., Low, F. J., et al. 2004, *ApJS*, 154, 1
- Whittet, D. C. B., Prusti, T., Franco, G. A. P., et al. 1997, *A&A*, 327, 1194
- Woitke, P., Kamp, I., & Thi, W. 2009, *A&A*, 501, 383
- Young, C. H., Jørgensen, J. K., Shirley, Y. L., et al. 2004, *ApJS*, 154, 396

Table 1. Source list

Embedded sources						
#	Source	RA	Dec	AOR	tint [s] (SL/SH/LH)*ndith.	D ^a [pc]
1	LDN1448 IRS1	3 ^h 25 ^m 09 ^s .4	30° 46′ 21″.7	5656832	(14*1/31*2/60*1)*2	250
2	LDN1448 NA	3 ^h 25 ^m 36 ^s .5	30° 45′ 21″.2	5828096	(60*1/121*2/60*1)*2	250
3	IRAS 03245+3002	3 ^h 27 ^m 39 ^s .0	30° 12′ 59″.4	6368000	(14*4/31*4/60*1)*2	250
4	L1455 SMM1	3 ^h 27 ^m 43 ^s .2	30° 12′ 28″.8	15917056	(60*2/121*2/-)*2	250
5	L1455 IRS3	3 ^h 28 ^m 00 ^s .4	30° 08′ 01″.3	15917568	(14*4/121*2/-)*2	250
6	IRAS 03254+3050	3 ^h 28 ^m 34 ^s .5	31° 00′ 51″.1	11827200	(14*2/31*2/60*1)*2	250
7	IRAS 03271+3013	3 ^h 30 ^m 15 ^s .2	30° 23′ 48″.8	5634304	(14*2/31*4/60*1)*2	250
8	IRAS 03301+3111	3 ^h 33 ^m 12 ^s .8	31° 21′ 24″.1	5634560	(14*1/6*2/14*2)*2	250
9	B1-a	3 ^h 33 ^m 16 ^s .7	31° 07′ 55″.2	15918080	(14*4/31*2/-)*2	250
10	B1-c	3 ^h 33 ^m 17 ^s .9	31° 09′ 31″.0	13460480	(14*2/-)*2	250
11	SSTc2d J033327.3+310710	3 ^h 33 ^m 27 ^s .3	31° 07′ 10″.2	15918336	(60*3/121*2/-)*2	250
12	HH 211-mm	3 ^h 43 ^m 56 ^s .8	32° 00′ 50″.4	5826304	(-31*2/60*2)*2	250
13	IRAS 03439+3233	3 ^h 47 ^m 05 ^s .4	32° 43′ 08″.4	5635072	(14*1/121*2/60*1)*2	250
14	IRAS 03445+3242	3 ^h 47 ^m 41 ^s .6	32° 51′ 43″.9	5635328	(14*1/6*2/14*1)*2	250
15	IRAS 08242-5050	8 ^h 25 ^m 43 ^s .8	-51° 00′ 35″.6	5638912	(14*1/6*2/14*1)*2	460
16	IRAS 08261-5100	8 ^h 27 ^m 38 ^s .9	-51° 10′ 37″.2	5638912	(14*1/6*2/14*1)*2	400
17	Ced 110 IRS4	11 ^h 06 ^m 46 ^s .6	-77° 22′ 32″.5	5639680/12692224	(-121*2/60*2)*2	178
18	Ced 110 IRS6	11 ^h 07 ^m 09 ^s .2	-77° 23′ 04″.2	5639680/12696832	(-121*2/60*2)*2	178
19	IRAS 12553-7651	12 ^h 59 ^m 06 ^s .6	-77° 07′ 40″.1	9830912	(14*1/31*1/60*1)*2	178
20	IRAS 15398-3359	15 ^h 43 ^m 02 ^s .3	-34° 09′ 06″.8	5828864	(14*2/31*6/60*1)*2	100
21	GSS30-IRS1	16 ^h 26 ^m 21 ^s .4	-24° 23′ 04″.2	5647616/12699392	(-31*1/14*2)*2	125
22	GY23	16 ^h 26 ^m 24 ^s .1	-24° 24′ 48″.2	5647616/12699136	(-31*1/14*2)*2	125
23	VLA 1623-243	16 ^h 26 ^m 26 ^s .4	-24° 24′ 30″.2	9828096/12695040	(-121*4/60*4)*2	125
24	WL12	16 ^h 26 ^m 44 ^s .2	-24° 34′ 48″.4	5647616/12699136	(-31*1/14*2)*2	125
25	IRS37	16 ^h 27 ^m 17 ^s .6	-24° 28′ 56″.6	5647616/12698880	(-31*1/14*2)*2	125
26	WL6	16 ^h 27 ^m 21 ^s .8	-24° 29′ 53″.2	5647616/12698880	(-31*1/14*2)*2	125
27	Elias32	16 ^h 27 ^m 28 ^s .4	-24° 27′ 21″.2	12664320/12698624	(-31*2/60*2)*2	125
28	VSSG17	16 ^h 27 ^m 30 ^s .2	-24° 27′ 43″.6	5647616/12698624	(-31*1/14*2)*2	125
29	IRS63	16 ^h 31 ^m 35 ^s .7	-24° 01′ 29″.6	9827840/12676608	(-31*1/14*1)*2	125
30	L1689-IRS5	16 ^h 31 ^m 52 ^s .1	-24° 56′ 15″.4	12664064/12704256	(-31*1/60*1)*2	125
31	IRAS 16293-2422B	16 ^h 32 ^m 22 ^s .6	-24° 28′ 32″.2	15735808	(60*1/121*4/60*4)*2	125
32	IRAS 16293-2422	16 ^h 32 ^m 22 ^s .9	-24° 28′ 36″.1	11826944	(60*1/121*4/60*4)*2	125
33	RNO 91	16 ^h 34 ^m 29 ^s .3	-15° 47′ 01″.3	5650432	(14*1/31*1/14*2)*2	140
34	SSTc2d J182916.2+01822	18 ^h 29 ^m 16 ^s .2	0° 18′ 22″.7	13210112	(14*1/31*2/-)*2	260
35	Serp-S68N	18 ^h 29 ^m 48 ^s .1	1° 16′ 42″.6	9828608	(-121*4/60*4)*2	260
36	Serp-SMM4	18 ^h 29 ^m 56 ^s .6	1° 13′ 15″.2	9828608	(-121*4/60*4)*2	260
37	EC88	18 ^h 29 ^m 57 ^s .6	1° 13′ 00″.5	9407232	(14*1/121*1/60*2)*2	260
38	Serp-SMM3	18 ^h 29 ^m 59 ^s .2	1° 14′ 00″.2	9828608	(-121*4/60*4)*2	260
39	R CrA IRS5	19 ^h 01 ^m 48 ^s .0	-36° 57′ 21″.6	9835264	(14*1/6*2/-)*2	130
40	CrA IRS7 A	19 ^h 01 ^m 55 ^s .3	-36° 57′ 22″.0	9835008	(14*1/31*3/60*2)*2	170
41	CrA IRS7 B	19 ^h 01 ^m 56 ^s .4	-36° 57′ 28″.1	9835008	(14*1/31*3/60*2)*2	170
42	CrA IRAS32	19 ^h 02 ^m 58 ^s .7	-37° 07′ 34″.7	9832192	(60*1/31*8/-)*2	170
43	IRAS 23238+7401	23 ^h 25 ^m 46 ^s .7	74° 17′ 37″.3	9833728	(14*1/31*8/60*2)*2	250
Unknown sources						
#	Source	RA	Dec	AOR	tint [s] (SL/SH/LH)*ndith.	D ^a [pc]
44	IRAS 13546-3941	13 ^h 57 ^m 38 ^s .9	-39° 56′ 00″.2	5642752	(14*1/31*2/60*1)*2	630
45	WL19	16 ^h 27 ^m 11 ^s .7	-24° 38′ 32″.3	9829888/12692992	(-31*2/14*2)*2	125
46	IRAS 16544-1604	16 ^h 57 ^m 19 ^s .7	-16° 09′ 23″.8	5826816	(-14*4)*2	140
47	SSTc2d J182813.2+00313	18 ^h 28 ^m 13 ^s .2	0° 03′ 13″.0	13210368	(14*1/31*2/-)*2	260
48	SSTc2d J182849.4+00604	18 ^h 28 ^m 49 ^s .4	-0° 06′ 04″.7	13210624	(14*1/31*1/-)*2	260
49	SSTc2d J182901.8+02954	18 ^h 29 ^m 01 ^s .8	0° 29′ 54″.2	13210112	(14*1/31*2/-)*2	260
50	SSTc2d J182914.8+00424	18 ^h 29 ^m 14 ^s .8	-0° 04′ 23″.9	13210112	(14*1/31*2/-)*2	260
51	EC69	18 ^h 29 ^m 54 ^s .4	1° 15′ 01″.8	9407232	(14*1/121*1/60*2)*2	260
Disk sources						
#	Source	RA	Dec	AOR	tint [s] (SL/SH/LH)*ndith.	D ^a [pc]
52	VSSG1	16 ^h 26 ^m 18 ^s .9	-24° 28′ 19″.6	5647616/12699392	(-31*1/14*2)*2	125
53	IRS14	16 ^h 26 ^m 31 ^s .0	-24° 31′ 05″.2	12664576	(60*2/31*1/-)*2	125
54	OphE-MM3	16 ^h 27 ^m 05 ^s .9	-24° 37′ 08″.0	6370816	(60*5/31*8/60*2)*2	125
55	GY224	16 ^h 27 ^m 11 ^s .2	-24° 40′ 46″.6	9829888/12698880	(-31*2/14*2)*2	125
56	WL20S	16 ^h 27 ^m 15 ^s .6	-24° 38′ 45″.6	9829888	(-31*2/14*2)*2	125
57	IRS42	16 ^h 27 ^m 21 ^s .5	-24° 41′ 43″.1	5647616/12699648	(-31*1/14*2)*2	125
58	CRBR 2422.8-3423	16 ^h 27 ^m 24 ^s .6	-24° 41′ 03″.1	9346048	(14*1/121*1/241*2)*2	125
59	IRS46	16 ^h 27 ^m 29 ^s .4	-24° 39′ 16″.2	9829888/12698624	(-31*2/14*2)*2	125
60	IRS51	16 ^h 27 ^m 39 ^s .8	-24° 43′ 15″.2	9829888/12699648	(-31*2/14*2)*2	125
61	EC82	18 ^h 29 ^m 56 ^s .9	1° 14′ 46″.7	9407232	(14*1/121*1/60*2)*2	260

^aAssumed cloud distances; Chamaeleon (178 pc Whittet et al. 1997), Lupus I, IV (150 pc) and Lupus III (200 pc Comerón 2008),

Ophiuchus (125 pc de Geus et al. 1989), Perseus (250 pc, see discussion in Enoch et al. 2006), Taurus-Auriga (160 pc Kenyon et al. 1994), Serpens (260 pc Straizys et al. 1996)

Table 2. Source characteristics

Embedded sources									
#	Source	Warm H ₂	Hot H ₂	[Ne II]	[Fe II]	[Si II]	H ₂ O ^a	outflow ^b	source size
		ext.	src	src	ext.	ext.			[""]
1	LDN1448 IRS1				✓			y	–
2	LDN1448 NA	✓	✓	✓	✓			y	–
3	IRAS 03245+3002	✓	✓					y	3.1(1.5)
4	L1455 SMM1	✓	✓			–		n	0.2(0.2)
5	L1455 IRS3	✓				–	✓	n	–
6	IRAS 03254+3050							y	1.1(0.8)
7	IRAS 03271+3013	✓	✓		✓			y	0.2(0.2)
8	IRAS 03301+3111			✓				n	0.3(0.2)
9	B1-a	✓	✓	✓		–	✓	y	–
10	B1-c		✓			–		y	–
11	SSTc2d J033327.3	✓	✓	✓		–		y	0.3(0.2)
12	HH 211-mm	✓	–		✓	✓		y	ext
13	IRAS 03439+3233							n	–
14	IRAS 03445+3242				✓	✓		y	0.2(0.2)
15	IRAS 08242-5050			✓	✓			–	0.2(0.2)
16	IRAS 08261-5100	✓						–	0.5(0.4)
17	Ced 110 IRS4	✓	✓	✓	✓			y	–
18	Ced 110 IRS6						✓	–	0.6(0.5)
19	IRAS 12553-7651							n	–
20	IRAS 15398-3359		✓			✓		y	0.5(0.3)
21	GSS30-IRS1		✓					n	0.4(0.3)
22	GY23	✓					✓	n	0.6(0.5)
23	VLA 1623-243	✓				✓		y	7.5(2.8)
24	WL12		✓					n	0.1(0.1)
25	IRS37	✓		✓				n	–
26	WL6	✓	✓				✓	n	0.1(0.1)
27	Elias32	✓						n	–
28	VSSG17	✓					✓✓	n	–
29	IRS63						✓	n	0.2(0.2)
30	L1689-IRS5						✓✓	n	0.2(0.2)
31	IRAS 16293-2422B	✓			✓			n	ext
32	IRAS 16293-2422	✓						n	ext
33	RNO 91			✓			✓	–	0.4(0.3)
34	SSTc2d J182916.2					–	✓	y	–
35	Serp-S68N	✓	–			✓		c	–
36	Serp-SMM4	✓	–		✓	✓		c	ext
37	EC88						✓	c	1.2(0.9)
38	Serp-SMM3	✓	–		✓	✓		c	ext
39	R CrA IRS5			✓		–	✓	c	–
40	CrA IRS7 A		✓	✓				c	0.3(0.2)
41	CrA IRS7 B	✓	✓	✓				c	0.8(0.6)
42	CrA IRS32		✓	✓	✓	–		c	0.5(0.3)
43	IRAS 23238+7401			✓				c	0.9(0.7)
Unknown sources									
#	Source	Warm H ₂	Hot H ₂	[Ne II]	[Fe II]	[Si II]	H ₂ O ^a	outflow ^b	source size
		ext.	src	src	ext.	ext.			[""]
44	IRAS 13546-3941							–	0.6(0.3)
45	WL19	✓					✓	n	–
46	IRAS 16544-1604		–	–				–	–
47	SSTc2d J182813.2			✓		–		n	0.2(0.2)
48	SSTc2d J182849.4					–		n	–
49	SSTc2d J182901.8					–	✓✓	n	–
50	SSTc2d J182914.8					–		n	–
51	EC69	✓			✓	✓		c	ext
Disk sources									
#	Source	Warm H ₂	Hot H ₂	[Ne II]	[Fe II]	[Si II]	H ₂ O ^a	outflow ^b	source size
		ext.	src	src	ext.	ext.			[""]
52	VSSG1	✓	✓			✓	✓✓	n	–
53	IRS14	✓	✓			–		n	7.7(0.8)
54	OphE-MM3	✓						n	7.1(1.5)
55	GY224	✓	✓				✓✓	n	–
56	WL20S		–	✓	✓			n	0.6(0.2)
57	IRS42							n	–
58	CRBR 2422.8-3423	✓	✓					n	0.1(0.1)
59	IRS46							n	0.2(0.2)
60	IRS51							–	0.3(0.2)
61	EC82							c	0.4(0.3)

^aOne ✓ indicates a detection in one extraction; two ✓✓ indicates sources with detection in both the optimal extraction and the full aperture extraction.^bEvidence for the presence of outflows based on a visual inspection of *Spitzer*-IRAC images; yes, no or confused.

Table 3. Observed linefluxes and 1σ uncertainties ($10^{-16}\text{erg cm}^{-2} \text{s}^{-1}$)

Embedded sources										
#	Source	[Ne II]			[Ne III]			[Fe I] 24.04		
		src ^a	ext ^a	upp ^a	src	ext	upp	src	ext	upp
1	LDN1448 IRS1	–	–	(30/23)	–	–	(43/7)	–	–	(110/44)
2	LDN1448 NA	240	23	(20/3)	–	–	(40/28)	–	–	(140/99)
3	IRAS 03245+3002	–	–	(6/5)	–	–	(20/20)	–	–	(110/60)
4	L1455 SMM1	–	–	(10/8)	–	–	(9/2)	–	–	–
5	L1455 IRS3	–	–	(18/2)	–	–	(15/2)	–	–	–
6	IRAS 03254+3050	–	–	(24/13)	–	–	(31/4)	–	–	(94/83)
7	IRAS 03271+3013	–	–	(19/11)	–	–	(43/29)	–	–	(72/53)
8	IRAS 03301+3111	390	–	(76/60)	–	–	(87/76)	–	–	(170/69)
9	B1-a	150	–	(23/4)	–	–	(30/26)	–	–	–
10	B1-c	–	–	(19/17)	–	–	(20/16)	–	–	–
11	SSTc2d J033327.3	870	–	(22/11)	52	–	(11/1)	–	–	–
12	HH 211-mm	–	–	(6/6)	–	–	(4/4)	–	–	(11/10)
13	IRAS 03439+3233	–	–	(24/3)	–	–	(9/1)	–	–	(110/53)
14	IRAS 03445+3242	–	–	(110/89)	–	–	(90/72)	–	–	(150/87)
15	IRAS 08242-5050	–	–	(110/83)	–	–	(75/9)	–	–	(200/90)
16	IRAS 08261-5100	–	–	(130/96)	–	–	(76/46)	–	–	(120/50)
17	Ced 110 IRS4	180	–	(23/2)	–	–	(6/1)	–	–	(35/24)
18	Ced 110 IRS6	–	–	(22/2)	–	–	(21/15)	–	–	(73/35)
19	IRAS 12553-7651	–	–	(31/24)	–	–	(56/8)	–	–	(130/60)
20	IRAS 15398-3359	–	–	(22/18)	–	–	(46/10)	–	–	(160/76)
21	GSS30-IRS1	–	–	(640/330)	–	–	(1100/160)	–	–	(2400/1300)
22	GY23	–	–	(110/68)	–	–	(91/22)	–	–	(140/80)
23	VLA 1623-243	–	–	(5/1)	–	–	(2/2)	–	–	(52/48)
24	WL12	–	–	(130/53)	–	–	(200/170)	–	–	(330/92)
25	IRS37	290	–	(31/25)	–	–	(38/35)	–	–	(110/84)
26	WL6	–	–	(78/42)	–	–	(110/88)	–	–	(210/100)
27	Elias32	–	–	(43/5)	–	–	(38/32)	–	–	(270/19)
28	VSSG17	–	–	(63/31)	–	–	(79/12)	–	–	(170/130)
29	IRS63	–	–	(36/28)	–	–	(59/8)	–	–	(230/120)
30	L1689-IRS5	–	–	(89/57)	–	–	(120/16)	–	–	(200/100)
31	IRAS 16293-2422B	–	–	(4/4)	–	–	(0/0)	–	–	(35/35)
32	IRAS 16293-2422	–	–	(3/3)	–	–	(1/1)	–	150	(32/33)
33	RNO 91	710	280	(83/59)	–	–	(93/9)	–	–	(210/110)
34	SSTc2d J182916.2	–	–	(37/34)	–	–	(31/5)	–	–	–
35	Serp-S68N	–	–	(14/2)	–	–	(6/1)	–	–	(26/23)
36	Serp-SMM4	–	–	(3/3)	–	–	(1/1)	–	–	(5/5)
37	EC88	–	–	(22/3)	–	–	(42/7)	–	–	(90/58)
38	Serp-SMM3	–	11	(4/1)	–	–	(3/3)	–	–	(23/23)
39	R CrA IRS5	1700	110	(140/27)	–	–	(160/22)	–	–	–
40	CrA IRS7 A	3700	–	(120/69)	–	–	(420/39)	–	–	(1500/680)
41	CrA IRS7 B	960	71	(45/15)	–	–	(100/10)	–	–	(560/380)
42	CrA IRAS32	200	–	(18/3)	–	–	(23/20)	–	–	–
43	IRAS 23238+7401	150	–	(22/12)	–	–	(54/12)	–	–	(130/61)
Unknown sources										
#	Source	[Ne II]			[Ne III]			[Fe I] 24.04		
		src ^a	ext ^a	upp ^a	src	ext	upp	src	ext	upp
44	IRAS 13546-3941	–	–	(27/3)	–	–	(28/4)	–	–	(53/48)
45	WL19	–	–	(25/20)	–	–	(19/3)	–	–	(73/30)
46	IRAS 16544-1604	–	–	–	–	–	–	–	–	(100/74)
47	SSTc2d J182813.2	130	–	(24/20)	–	–	(26/19)	–	–	–
48	SSTc2d J182849.4	–	–	(100/75)	–	–	(66/57)	–	–	–
49	SSTc2d J182901.8	–	–	(43/6)	–	–	(23/18)	–	–	–
50	SSTc2d J182914.8	–	–	(35/31)	–	–	(29/25)	–	–	–
51	EC69	–	–	(4/4)	–	–	(1/1)	–	–	(4/4)
Disk sources										
#	Source	[Ne II]			[Ne III]			[Fe I] 24.04		
		src ^a	ext ^a	upp ^a	src	ext	upp	src	ext	upp
52	VSSG1	–	–	(76/49)	–	–	(65/10)	–	–	(130/77)
53	IRS14	–	–	(9/9)	–	–	(6/6)	–	–	–
54	OphE-MM3	–	–	(5/5)	–	–	(4/4)	–	–	(63/37)
55	GY224	–	–	(28/3)	–	–	(34/5)	–	–	(69/34)
56	WL20S	460	–	(44/32)	–	–	(52/8)	–	–	(230/100)
57	IRS42	–	–	(150/35)	–	–	(98/17)	–	–	(540/86)
58	CRBR 2422.8-3423	–	–	(18/3)	–	–	(16/4)	–	–	(63/47)
59	IRS46	–	–	(38/23)	–	–	(36/8)	–	–	(170/78)
60	IRS51	–	–	(63/7)	–	–	(55/11)	–	–	(160/66)
61	EC82	–	–	(51/9)	–	–	(66/11)	–	–	(110/76)

^asrc = compact (or slightly extended, see Table 2) component centered on source ; ext = fully extended (to *Spitzer*-IRS) component ; upp = 1σ upper limit of src/ext linefluxes

Table 3. – continued –

Embedded sources												
#	[Fe II] 17.94			[Fe II] 25.99			[S I]			[Si II]		
	src	ext	upp	src	ext	upp	src	ext	upp	src	ext	upp
1	370	–	(91/20)	350	360	(83/57)	–	–	(63/43)	670	–	(99/57)
2	–	–	(50/12)	1300	920	(300/150)	–	–	(150/100)	–	–	(210/140)
3	–	–	(28/25)	–	–	(110/75)	–	–	(140/83)	–	–	(390/30)
4	–	–	(24/5)	–	–	–	–	–	–	–	–	–
5	–	–	(19/4)	–	–	–	–	–	–	–	–	–
6	–	–	(30/20)	–	–	(60/40)	–	–	(59/45)	–	–	(190/160)
7	–	–	(29/25)	–	36	(82/8)	–	–	(61/47)	–	–	(140/91)
8	–	–	(100/20)	–	–	(93/64)	–	–	(110/58)	–	–	(150/110)
9	–	–	(47/45)	–	–	–	–	–	–	–	–	–
10	–	–	(26/24)	–	–	–	–	–	–	–	–	–
11	160	–	(25/3)	–	–	–	–	–	–	–	–	–
12	–	–	(2/2)	–	110	(5/5)	–	100	(6/7)	–	100	(39/19)
13	–	–	(20/19)	–	–	(44/32)	–	–	(45/35)	–	–	(110/82)
14	480	–	(110/30)	1500	–	(130/110)	–	–	(130/94)	2200	100	(180/22)
15	–	–	(150/38)	–	860	(230/150)	–	–	(170/120)	–	–	(340/220)
16	–	–	(88/19)	–	–	(110/67)	–	–	(110/53)	–	–	(170/130)
17	–	16	(16/2)	–	280	(48/29)	–	–	(29/18)	–	–	(76/51)
18	–	–	(41/38)	–	–	(42/22)	–	–	(63/30)	–	–	(110/93)
19	–	–	(59/54)	–	–	(86/67)	–	–	(78/34)	–	–	(160/91)
20	–	–	(36/7)	620	–	(89/82)	–	–	(100/92)	–	520	(140/100)
21	–	–	(1400/1200)	–	–	(1800/1200)	–	–	(1600/660)	–	–	(2000/1400)
22	–	–	(110/110)	–	–	(95/7)	–	–	(140/78)	–	–	(170/160)
23	–	–	(2/2)	–	–	(52/4)	–	–	(28/3)	–	56	(150/13)
24	–	–	(170/150)	–	–	(210/150)	–	–	(260/150)	–	–	(330/26)
25	–	–	(57/11)	–	–	(110/93)	–	–	(100/83)	–	–	(240/23)
26	–	–	(88/80)	–	–	(140/90)	–	–	(200/120)	780	–	(180/140)
27	–	–	(49/41)	–	–	(57/40)	–	–	(74/6)	–	–	(73/64)
28	–	–	(50/31)	–	–	(72/59)	–	–	(100/67)	660	–	(93/81)
29	–	–	(85/76)	–	–	(120/76)	–	–	(140/66)	–	–	(240/170)
30	–	–	(140/130)	–	–	(130/110)	–	–	(150/100)	–	–	(180/150)
31	–	–	(3/2)	–	–	(77/69)	–	460	(47/47)	–	–	(470/310)
32	–	–	(4/4)	–	–	(60/60)	–	200	(30/30)	–	–	(250/250)
33	–	–	(76/60)	–	–	(160/100)	–	–	(240/130)	–	–	(330/26)
34	–	–	(40/37)	–	–	–	–	–	–	–	–	–
35	–	–	(10/8)	–	–	(30/20)	220	160	(44/34)	–	37	(67/7)
36	–	16	(2/2)	160	260	(13/6)	–	260	(580/29)	–	1100	(54/63)
37	–	–	(80/16)	–	–	(80/47)	–	–	(73/64)	–	–	(150/100)
38	–	67	(6/6)	–	150	(13/13)	–	450	(28/27)	–	600	(56/85)
39	–	–	(210/190)	–	–	–	–	–	–	–	–	–
40	–	–	(400/370)	–	–	(1400/220)	–	–	(1700/1300)	–	–	(2700/2200)
41	–	–	(160/29)	2700	–	(500/340)	–	–	(340/200)	–	–	(1100/750)
42	640	150	(48/36)	–	–	–	–	–	–	–	–	–
43	–	–	(17/4)	–	–	(68/42)	–	–	(77/47)	–	–	(150/140)

Unknown sources												
#	[Fe II] 17.94			[Fe II] 25.99			[S I]			[Si II]		
	src	ext	upp	src	ext	upp	src	ext	upp	src	ext	upp
44	–	–	(38/26)	–	–	(59/39)	–	–	(62/49)	–	–	(67/51)
45	–	–	(35/34)	–	–	(44/30)	–	–	(54/3)	–	–	(130/12)
46	–	–	–	–	–	(120/99)	–	–	(85/70)	–	–	(290/190)
47	–	–	(30/24)	–	–	–	–	–	–	–	–	–
48	–	–	(44/38)	–	–	–	–	–	–	–	–	–
49	–	–	(28/25)	–	–	–	–	–	–	–	–	–
50	–	–	(22/4)	–	–	–	–	–	–	–	–	–
51	–	–	(11/11)	–	21	(3/3)	–	–	(1/1)	–	120	(12/12)

Disk sources												
#	[Fe II] 17.94			[Fe II] 25.99			[S I]			[Si II]		
	src	ext	upp	src	ext	upp	src	ext	upp	src	ext	upp
52	–	–	(69/61)	–	–	(54/46)	–	–	(83/47)	–	1200	(150/140)
53	–	–	(18/18)	–	–	–	–	–	–	–	–	–
54	–	–	(11/10)	–	–	(30/3)	–	–	(35/3)	–	–	(120/120)
55	–	–	(40/9)	–	–	(78/6)	–	–	(82/73)	–	–	(110/73)
56	–	160	(170/39)	2200	130	(230/32)	–	–	(330/150)	2000	–	(340/230)
57	–	–	(110/100)	–	–	(140/130)	–	–	(120/9)	–	–	(140/89)
58	–	–	(37/33)	–	–	(50/41)	–	–	(52/4)	–	–	(77/43)
59	–	–	(52/45)	–	–	(94/9)	–	–	(85/9)	–	–	(260/29)
60	–	–	(77/71)	–	–	(75/52)	–	–	(140/100)	–	–	(180/14)
61	–	–	(140/130)	–	–	(89/73)	–	–	(110/85)	–	–	(160/98)

Table 4. Observed linefluxes and 1σ uncertainties ($10^{-16}\text{erg cm}^{-2} \text{s}^{-1}$)

Embedded sources													
#	Source	H2 S(0)			H2 S(1)			H2 S(2)			H2 S(3)		
		src ^a	ext ^a	upp ^a	src	ext	upp	src	ext	upp	src	ext	upp
1	LDN1448 IRS1	–	–	(110/71)	–	–	(51/45)	–	–	(42/37)	–	–	(140/35)
2	LDN1448 NA	–	–	(190/150)	–	–	(31/58)	–	77	(26/3)	–	76	(130/4)
3	IRAS 03245+3002	–	–	(240/130)	–	14	(11/2)	–	–	(14/12)	–	–	(13/4)
4	L1455 SMM1	–	–	–	–	17	(8/1)	–	–	(14/12)	–	14	(7/3)
5	L1455 IRS3	–	–	–	–	–	(18/2)	–	15	(25/3)	–	–	(33/22)
6	IRAS 03254+3050	–	–	(80/64)	–	–	(28/23)	–	–	(33/26)	–	–	(52/18)
7	IRAS 03271+3013	–	–	(73/58)	–	24	(27/5)	–	–	(32/17)	–	25	(41/3)
8	IRAS 03301+3111	–	–	(240/83)	–	–	(100/77)	–	–	(90/72)	–	–	(210/60)
9	B1-a	–	–	–	–	–	(34/5)	–	33	(33/6)	–	40	(38/8)
10	B1-c	–	–	–	–	–	(17/15)	–	–	(20/16)	–	–	(27/9)
11	SSTc2d J033327.3	–	–	–	–	73	(13/13)	–	17	(16/2)	68	16	(9/2)
12	HH 211-mm	–	150	(9/8)	–	67	(2/2)	–	46	(4/4)	–	–	–
13	IRAS 03439+3233	–	–	(64/39)	–	–	(14/2)	–	–	(14/13)	–	68	(71/13)
14	IRAS 03445+3242	–	–	(120/89)	–	–	(67/60)	–	–	(80/45)	–	–	(250/67)
15	IRAS 08242-5050	–	–	(250/210)	–	–	(99/80)	–	–	(70/56)	–	–	(810/350)
16	IRAS 08261-5100	–	420	(130/69)	–	–	(96/61)	–	–	(96/17)	–	–	(200/98)
17	Ced 110 IRS4	–	–	(54/40)	–	23	(12/2)	–	–	(7/6)	–	–	(37/14)
18	Ced 110 IRS6	–	–	(76/43)	–	–	(34/30)	–	–	(12/11)	–	–	(210/110)
19	IRAS 12553-7651	–	–	(100/100)	–	–	(57/53)	–	–	(40/33)	–	–	(100/17)
20	IRAS 15398-3359	–	–	(76/68)	–	–	(23/4)	–	–	(31/29)	–	–	(68/30)
21	GSS30-IRS1	–	–	(1700/1100)	–	–	(990/960)	–	–	(540/400)	–	–	(1800/120)
22	GY23	690	–	(130/130)	–	88	(74/13)	–	–	(100/85)	–	–	(630/490)
23	VLA 1623-243	–	66	(81/7)	–	110	(2/2)	–	58	(3/3)	–	–	(7/3)
24	WL12	–	–	(290/190)	–	–	(140/25)	–	–	(130/86)	–	–	(320/190)
25	IRS37	–	48	(73/5)	–	27	(33/5)	–	–	(28/23)	–	–	(59/25)
26	WL6	–	530	(270/91)	–	–	(89/18)	–	–	(110/70)	–	–	(390/65)
27	Elias32	–	–	(100/6)	–	27	(36/6)	–	–	(37/34)	–	–	(270/180)
28	VSSG17	–	62	(110/8)	–	–	(58/12)	–	–	(88/49)	–	–	(700/430)
29	IRS63	–	–	(160/110)	–	–	(65/59)	–	–	(69/39)	–	–	(310/140)
30	L1689-IRS5	–	–	(130/120)	–	–	(180/140)	–	–	(100/72)	–	–	(640/240)
31	IRAS 16293-2422B	–	–	(99/99)	–	66	(1/1)	–	33	(5/5)	–	–	(4/4)
32	IRAS 16293-2422	–	110	(66/20)	–	63	(1/1)	–	34	(1/1)	–	–	(3/3)
33	RNO 91	–	–	(230/180)	–	–	(96/87)	330	–	(81/64)	–	–	(530/210)
34	SSTc2d J182916.2	–	–	–	–	–	(39/6)	–	–	(48/36)	–	–	(110/16)
35	Serp-S68N	–	–	(49/3)	–	44	(8/9)	–	–	(4/3)	–	–	–
36	Serp-SMM4	–	120	(23/10)	–	81	(2/5)	–	190	(5/13)	–	–	–
37	EC88	–	–	(110/97)	–	–	(39/12)	–	–	(27/3)	–	–	(4600/4600)
38	Serp-SMM3	–	97	(37/10)	–	160	(3/3)	–	150	(3/3)	–	–	–
39	R CrA IRS5	–	–	–	–	–	(160/140)	–	–	(150/130)	–	–	(670/260)
40	CrA IRS7 A	–	–	(2900/200)	–	–	(600/420)	–	–	(130/120)	–	–	(280/24)
41	CrA IRS7 B	–	–	(730/530)	–	–	(120/22)	–	66	(65/13)	–	–	(190/89)
42	CrA IRAS32	–	–	–	–	–	(15/3)	–	–	(19/16)	34	7	(7/1)
43	IRAS 23238+7401	–	–	(80/30)	–	–	(13/8)	–	–	(10/7)	–	–	(32/9)
Unknown sources													
#	Source	H2 S(0)			H2 S(1)			H2 S(2)			H2 S(3)		
		src ^a	ext ^a	upp ^a	src	ext	upp	src	ext	upp	src	ext	upp
44	IRAS 13546-3941	–	–	(78/41)	–	–	(31/20)	–	–	(27/16)	–	–	(200/140)
45	WL19	–	21	(51/3)	–	–	(22/4)	–	–	(20/14)	–	–	(54/18)
46	IRAS 16544-1604	–	–	(82/67)	–	–	–	–	–	–	–	–	–
47	SSTc2d J182813.2	–	–	–	–	–	(27/5)	–	–	(26/21)	–	–	(170/12)
48	SSTc2d J182849.4	–	–	–	–	–	(55/46)	–	–	(67/48)	–	–	(630/120)
49	SSTc2d J182901.8	–	–	–	–	–	(35/7)	–	–	(100/99)	–	330	(190/69)
50	SSTc2d J182914.8	–	–	–	–	–	(12/11)	–	–	(86/85)	–	–	(130/30)
51	EC69	–	100	(3/3)	–	60	(2/2)	–	34	(3/3)	–	–	(20/20)
Disk sources													
#	Source	H2 S(0)			H2 S(1)			H2 S(2)			H2 S(3)		
		src ^a	ext ^a	upp ^a	src	ext	upp	src	ext	upp	src	ext	upp
52	VSSG1	750	–	(120/110)	–	530	(85/130)	–	390	(88/66)	–	–	(360/72)
53	IRS14	–	–	–	–	790	(11/11)	–	450	(18/18)	–	–	(39/37)
54	OphE-MM3	–	–	(41/36)	–	3	(2/0)	–	–	(5/5)	–	–	(10/1)
55	GY224	–	30	(87/5)	–	–	(44/6)	–	–	(29/15)	–	–	(170/25)
56	WL20S	–	–	(180/120)	–	–	(76/14)	–	–	(44/37)	–	–	–
57	IRS42	–	–	(97/90)	–	–	(68/19)	–	–	(110/63)	–	–	(910/600)
58	CRBR 2422.8-3423	–	–	(95/7)	–	–	(27/5)	–	14	(13/3)	–	–	(34/13)
59	IRS46	–	–	(130/10)	–	–	(38/7)	–	–	(41/30)	–	–	(250/85)
60	IRS51	–	–	(170/130)	–	–	(77/14)	–	–	(35/21)	–	–	(950/580)
61	EC82	–	–	(180/140)	–	–	(120/21)	–	–	(52/13)	–	–	(1200/230)

^asee footnote a of Table 3

Table 4. – continued –

Embedded sources												
#	H2 S(4)			H2 S(5)			H2 S(6)			H2 S(7)		
	src	ext	upp	src	ext	upp	src	ext	upp	src	ext	upp
1	–	–	(330/40)	–	–	(160/0)	–	–	(160/0)	–	–	(190/0)
2	1100	210	(250/23)	–	440	(270/57)	–	–	(220/0)	–	350	(670/80)
3	230	–	(55/11)	–	–	(51/0)	–	–	(100/0)	–	–	(160/0)
4	360	–	(84/2)	210	–	(34/0)	–	–	(53/0)	–	–	(150/0)
5	–	–	(100/12)	–	–	–	–	–	–	–	–	–
6	–	–	(100/43)	–	–	(320/0)	–	–	(190/0)	–	–	(120/0)
7	320	–	(48/14)	550	–	(77/0)	230	–	(54/0)	320	–	(46/0)
8	–	–	(320/110)	–	–	(230/0)	–	–	(170/0)	–	–	(190/0)
9	910	–	(200/15)	–	–	(260/0)	–	–	(140/0)	3400	–	(770/0)
10	6000	250	(1200/62)	–	–	(480/0)	–	–	(430/0)	–	–	(500/0)
11	150	–	(10/4)	–	–	(110/0)	–	–	(38/0)	470	–	(45/0)
12	–	–	–	–	–	–	–	–	–	–	–	–
13	–	–	(90/35)	–	–	(94/0)	–	–	(100/0)	–	–	(90/0)
14	–	–	(1600/61)	–	–	(510/0)	–	–	(570/0)	–	–	(570/0)
15	–	–	(950/64)	–	–	(1300/0)	–	–	(1000/0)	–	–	(1100/0)
16	–	–	(210/68)	–	–	(200/0)	–	–	(210/0)	–	–	(260/0)
17	250	–	(58/16)	–	–	–	–	–	–	–	–	–
18	–	130	(390/25)	–	–	–	–	–	–	–	–	–
19	–	–	(1700/100)	–	–	(320/0)	–	–	(410/0)	–	–	(390/0)
20	400	–	(86/27)	–	–	(160/0)	–	–	(200/0)	–	–	(190/0)
21	27000	–	(5800/350)	–	–	–	–	–	–	–	–	–
22	–	–	(3300/92)	–	–	–	–	–	–	–	–	–
23	–	–	(7/4)	–	–	–	–	–	–	–	–	–
24	9800	–	(2300/75)	–	–	–	–	–	–	–	–	–
25	–	–	(300/35)	–	–	–	–	–	–	–	–	–
26	9000	–	(1600/140)	–	–	–	–	–	–	–	–	–
27	–	–	(610/23)	–	–	–	–	–	–	–	–	–
28	–	–	(2700/35)	–	–	–	–	–	–	–	–	–
29	–	–	(2100/54)	–	–	–	–	–	–	–	–	–
30	–	–	(1700/290)	–	–	–	–	–	–	–	–	–
31	–	43	(5/6)	–	67	(15/15)	–	–	(14/14)	–	–	(15/13)
32	–	18	(4/4)	–	–	(16/15)	–	–	(15/16)	–	–	(27/27)
33	–	–	(1300/97)	–	–	(1100/0)	–	–	(1600/0)	–	–	(1600/0)
34	–	–	(180/130)	–	–	(150/89)	–	–	(180/120)	–	–	(320/240)
35	–	–	–	–	–	–	–	–	–	–	–	–
36	–	–	–	–	–	–	–	–	–	–	–	–
37	–	–	(8200/8200)	–	–	(250/0)	–	–	(390/0)	–	–	(410/0)
38	–	–	–	–	–	–	–	–	–	–	–	–
39	–	–	(1300/100)	–	–	(1000/0)	–	–	(840/0)	–	–	(1100/0)
40	4900	–	(1200/280)	–	–	(3000/0)	–	–	(720/0)	–	–	(690/0)
41	4200	–	(1000/130)	–	–	(830/0)	–	–	(720/0)	–	–	(790/0)
42	90	–	(11/2)	–	–	(92/0)	–	–	(60/0)	–	–	(71/0)
43	–	–	(250/19)	–	–	(130/0)	–	–	(110/0)	–	–	(120/72)
Unknown sources												
#	H2 S(4)			H2 S(5)			H2 S(6)			H2 S(7)		
	src	ext	upp	src	ext	upp	src	ext	upp	src	ext	upp
44	–	–	(290/110)	–	–	(150/0)	–	–	(160/0)	–	–	(170/0)
45	–	–	(190/26)	–	–	–	–	–	–	–	–	–
46	–	–	–	–	–	–	–	–	–	–	–	–
47	–	–	(370/70)	–	–	(350/0)	–	–	(410/0)	–	–	(250/0)
48	–	–	(1100/870)	–	–	(1500/0)	–	–	(2000/0)	–	–	(1500/0)
49	–	–	(260/110)	–	–	(160/94)	–	–	(260/200)	–	–	(450/380)
50	–	–	(170/24)	–	–	(310/88)	–	–	(290/100)	–	–	(530/400)
51	–	–	(35/35)	–	–	(66/65)	–	–	(64/65)	–	–	(89/86)
Disk sources												
#	H2 S(4)			H2 S(5)			H2 S(6)			H2 S(7)		
	src	ext	upp	src	ext	upp	src	ext	upp	src	ext	upp
52	6600	–	(880/120)	–	–	–	–	–	–	–	–	–
53	33	–	(8/86)	–	–	(36/0)	–	–	(42/0)	–	–	(37/0)
54	–	–	(7/6)	–	–	(16/0)	–	–	(22/0)	–	–	(18/0)
55	2700	110	(190/24)	–	–	–	–	–	–	–	–	–
56	–	–	–	–	–	–	–	–	–	–	–	–
57	–	–	(2600/62)	–	–	–	–	–	–	–	–	–
58	550	–	(120/29)	–	–	(160/0)	–	–	(160/0)	–	–	(210/0)
59	–	–	(860/44)	–	–	–	–	–	–	–	–	–
60	–	–	(1500/36)	–	–	–	–	–	–	–	–	–
61	–	–	(910/310)	–	–	(360/0)	–	–	(770/0)	–	–	(520/0)

Table 5. Diagnostic parameters of the gas contents

Embedded sources														
#	Source	Warm H ₂ ^a						Hot H ₂ ^a						
		Compact ^b			Extended			Compact ^b			Extended			
		[K]	[10 ²² cm ⁻²]	[M _J]	[K]	[10 ²⁰ cm ⁻²]	[M _J]	[K]	[10 ²⁰ cm ⁻²]	[10 ⁻³ M _J]	[K]	[10 ¹⁸ cm ⁻²]	[10 ⁻³ M _J]	
1	LDN1448 IRS1	< 600	< 18.4		< 14	< 7.9		< 10	< 3.2			< 2	< 1.5	
2	LDN1448 NA	< 600	< 19.2		< 29	< 17.1		6	1.8		623	6	3.8	
3	IRAS 03245+3002	< 400	< 12.6		3	1.8		2	0.9			0.5	0.3	
4	L1455 SMM1	< 80	< 2.5		1	1.1		1	0.4			0.5	0.3	
5	L1455 IRS3	< 164	< 5.1		< 0.8	< 0.4		< 3	< 1.0			< 1	< 0.6	
6	IRAS 03254+3050	< 380	< 11.7		< 9	< 5.3		< 7	< 2.2			< 1	< 1.1	
7	IRAS 03271+3013	< 364	< 11.3		5	2.9		857	4	1.2		0.6	0.4	
8	IRAS 03301+3111	< 1280	< 39.1		< 20	< 12.0		< 13	< 4.3			< 6	< 3.6	
9	B1-a	< 308	< 9.6		< 2	< 1.4		4	1.5		615	3	1.8	
10	B1-c	< 124	< 3.8		< 6	< 3.8		6	2.1			< 1	< 1.1	
11	SSTc2d J033327.3	< 104	< 3.2		10	5.6		1514	1	0.4		539	2	1.1
12	HH 211-mm	< 37	< 1.2		5	2.8		< 1	< 0.4			3	2.1	
13	IRAS 03439+3233	< 244	< 7.5		< 2	< 1.6		< 3	< 1.0			< 1	< 0.6	
14	IRAS 03445+3242	< 680	< 21.2		< 20	< 11.1		< 27	< 8.7			< 4	< 2.5	
15	IRAS 08242-5050	< 4000	< 126.5		< 34	< 64.5		< 152	< 47.1			< 11	< 21.8	
16	IRAS 08261-5100	< 2280	< 70.5		20	28.5		< 32	< 9.9			4	6.5	
17	Ced 110 IRS4	< 104	< 3.3		2	0.8		1	0.3			1	0.3	
18	Ced 110 IRS6	< 212	< 6.5		< 8	< 2.4		< 4	< 1.3			< 5	< 1.5	
19	IRAS 12553-7651	< 300	< 9.3		< 19	< 5.5		< 8	< 2.7			< 2	< 0.8	
20	IRAS 15398-3359	< 56	< 1.7		< 5	< 0.5		1	0.3			< 1	< 0.1	
21	GSS30-IRS1	< 2640	< 81.4		< 309	< 43.4		48	14.3			< 25	< 3.5	
22	GY23	240	7.4		10	1.4		< 11	< 3.6			13	1.8	
23	VLA 1623-243	< 29	< 0.9		142	< 0.9	< 0.1	< 0.1	< 0.0			7	1.1	
24	WL12	< 396	< 12.3		< 19	< 2.7		10	3.4			< 8	< 1.2	
25	IRS37	< 100	< 3.1		1	0.3		< 1	< 0.5			2	0.3	
26	WL6	< 300	< 9.3		16	2.3		10	3.3			6	0.9	
27	Elias32	< 120	< 3.7		0.9	0.1		< 3	< 1.1			5	0.8	
28	VSSG17	< 144	< 4.5		2	0.3		< 10	< 3.3			9	1.3	
29	IRS63	< 196	< 6.1		< 22	< 3.1		< 7	< 2.3			< 6	< 0.9	
30	L1689-IRS5	< 288	< 8.9		< 29	< 4.3		10	3.2			< 20	< 2.9	
31	IRAS 16293-2422B	< 26	< 0.8	> 100	< 8	< 1.1		< 0.1	< 0.0		777	2	0.3	
32	IRAS 16293-2422	< 20	< 0.6	109	< 2	< 0.4		< 0.1	< 0.0		522	5	0.7	
33	RNO 91	< 356	< 11.0		< 33	< 5.9		17	5.3			< 8	< 1.5	
34	SSTc2d J182916.2	< 400	< 12.8		< 1	< 1.2		< 8	< 2.5			< 2	< 1.7	
35	Serp-S68N	< 176	< 5.4		0.7	0.4		< 1	< 0.4			3	1.9	
36	Serp-SMM4	< 68	< 2.1		4	2.6		< 1	< 0.5			11	6.7	
37	EC88	< 520	< 16.4		< 9	< 5.7		< 40	< 12.5			< 25	< 15.0	
38	Serp-SMM3	< 96	< 3.0	177	< 0.7	< 0.2		< 1	< 0.3			34	7.4	
39	R CrA IRS5	< 340	< 10.5		< 65	< 9.9		< 13	< 4.2			< 13	< 1.9	
40	CrA IRS7 A	< 5200	< 155.7		< 85	< 22.2		22	7.0			< 7	< 1.9	
41	CrA IRS7 B	< 1080	< 33.9		< 31	< 8.0		12	4.0			< 4	< 1.2	
42	CrA IRAS32	< 68	< 2.1		< 1	< 0.4	621	1	0.5			< 0.3	< 0.1	
43	IRAS 23238+7401	< 260	< 8.1		< 4	< 2.6		< 4	< 1.4			< 0.9	< 0.5	
Unknown sources														
#	Source	Warm H ₂ ^a						Hot H ₂ ^a						
		Compact ^b			Extended			Compact ^b			Extended			
		[K]	[10 ²² cm ⁻²]	[M _J]	[K]	[10 ²⁰ cm ⁻²]	[M _J]	[K]	[10 ²⁰ cm ⁻²]	[10 ⁻³ M _J]	[K]	[10 ¹⁸ cm ⁻²]	[10 ⁻³ M _J]	
44	IRAS 13546-3941	< 2440	< 76.0		< 6	< 23.1		< 60	< 18.2			< 5	< 19.3	
45	WL19	< 68	< 2.1		0.9	0.1		< 1	< 0.4			1	0.3	
46	IRAS 16544-1604	< 0.0	< 0.0		< 0.0	< 0.0		< 0.0	< 0.0			< 0.0	< 0.0	
47	SSTc2d J182813.2	< 184	< 5.7		< 1	< 0.8		< 14	< 4.6			< 2	< 1.3	
48	SSTc2d J182849.4	< 88	< 2.7		< 17	< 10.3		< 64	< 19.9			< 12	< 7.5	
49	SSTc2d J182901.8	< 308	< 9.5		< 0.0	< 0.0		< 10	< 3.2			< 6	< 3.9	
50	SSTc2d J182914.8	< 3	< 0.1		< 4	< 2.6		< 15	< 4.8			< 2	< 1.7	
51	EC69	< 20	< 0.6		110	2	1.7	< 2	< 0.7			4	2.4	
Disk sources														
#	Source	Warm H ₂ ^a						Hot H ₂ ^a						
		Compact ^b			Extended			Compact ^b			Extended			
		[K]	[10 ²² cm ⁻²]	[M _J]	[K]	[10 ²⁰ cm ⁻²]	[M _J]	[K]	[10 ²⁰ cm ⁻²]	[10 ⁻³ M _J]	[K]	[10 ¹⁸ cm ⁻²]	[10 ⁻³ M _J]	
52	VSSG1	284	8.8		29	4.1		9	2.9			15	2.1	
53	IRS14	< 24	< 0.7	> 100	< 90	< 12.7		0.5	0.1			27	3.8	
54	OphE-MM3	< 20	< 0.6		1	0.2		< 0.2	< 0.1			0.3	0.0	
55	GY224	< 120	< 3.7		1	0.2		4	1.5			2	0.3	
56	WL20S	< 240	< 7.4		< 11	< 1.6		< 3	< 0.9			< 5	< 0.8	
57	IRS42	< 140	< 4.4		< 10	< 1.4		< 12	< 3.9			< 14	< 2.0	
58	CRBR 2422.8-3423	< 104	< 3.2		< 1	< 0.2		1	0.5			< 1	< 0.1	
59	IRS46	< 140	< 4.4		< 1	< 0.2		< 4	< 1.4			< 5	< 0.7	
60	IRS51	< 220	< 6.9		< 11	< 1.6		< 8	< 2.5			< 10	< 1.4	
61	EC82	< 1200	< 37.7		< 14	< 8.8		< 35	< 10.9			< 7	< 4.6	

^a100 K is assumed for the warm component and 1000 K for the hot component. The derived column density and mass of the warm component depend strongly on the assumed temperature. A temperature of 150 and 200 K reduces the column density and mass by respectively a factor of ~ 30 and 140. For the hot component 1500 K instead of 1000 K may results in a reduction of column density and mass up to a factor of 10.

^bFor the unresolved emission a source with $r = 50$ AU is assumed to obtain an estimate of the column density.